

SDSS-IV MaNGA: stellar rotational support in disc galaxies versus central surface density and stellar population age

Xiaohan Wang ^{1,2}★, Yifei Luo ²★, S. M. Faber ³, David C. Koo,³ Shude Mao ¹, Kyle B. Westfall ³, Shengdong Lu ⁴, Weichen Wang ⁵, Kevin Bundy,³ N. Boardman,⁶ Vladimir Avila-Reese ⁷, José G. Fernández-Trincado ⁸ and Richard R. Lane ^{9,10}

¹Department of Astronomy, Tsinghua University, Beijing 100084, China

²Department of Astronomy and Astrophysics, University of California at Santa Cruz, Santa Cruz, CA 95064, USA

³UCO/Lick Observatory, Department of Astronomy and Astrophysics, University of California, Santa Cruz, CA 95064, USA

⁴Institute for Computational Cosmology, Department of Physics, University of Durham, South Road, Durham, DH1 3LE, UK

⁵Dipartimento di Fisica G. Occhialini, Università degli Studi di Milano-Bicocca, Piazza della Scienza 3, I-20126 Milano, Italy

⁶School of Physics and Astronomy, University of St Andrews, North Haugh, St Andrews KY16 9SS, UK

⁷Instituto de Astronomía, Universidad Nacional Autónoma de México, A.P. 70-264, 04510 México D. F., México

⁸Instituto de Astronomía, Universidad Católica del Norte, Av. Angamos 0610, Antofagasta, Chile

⁹Centro de Investigación en Astronomía, Facultad de Ingeniería, Ciencia y Tecnología, Universidad Bernardo O'Higgins, Avenida Viel 1497, Santiago, Chile

¹⁰Escuela de Ingeniería Civil, Facultad de Ingeniería, Ciencia y Tecnología, Universidad Bernardo O'Higgins, Avenida Viel 1497, Santiago, Chile

Accepted 2024 August 1. Received 2024 July 16; in original form 2023 November 7

ABSTRACT

We investigate how the stellar rotational support changes as a function of spatially resolved stellar population age (D_n4000) and relative central stellar surface density ($\Delta\Sigma_1$) for MaNGA isolated/central disc galaxies. We find that the galaxy rotational support indicator λ_{R_c} varies smoothly as a function of $\Delta\Sigma_1$ and D_n4000 . D_n4000 versus $\Delta\Sigma_1$ follows a ‘J-shape’, with λ_{R_c} contributing to the scatters. In this ‘J-shaped’ pattern rotational support increases with central D_n4000 when $\Delta\Sigma_1$ is low but decreases with $\Delta\Sigma_1$ when $\Delta\Sigma_1$ is high. Restricting attention to low- $\Delta\Sigma_1$ (i.e. large-radius) galaxies, we suggest that the trend of increasing rotational support with D_n4000 for these objects is produced by a mix of two different processes, a primary trend characterized by growth in λ_{R_c} along with mass through gas accretion, on top of which disturbance episodes are overlaid, which reduce rotational support and trigger increased star formation. An additional finding is that star-forming galaxies with low $\Delta\Sigma_1$ have relatively larger radii than galaxies with higher $\Delta\Sigma_1$ at fixed stellar mass. Assuming that these relative radii rankings are preserved while galaxies are star forming then implies clear evolutionary paths in central D_n4000 versus $\Delta\Sigma_1$. The paper closes with comments on the implications that these paths have for the evolution of pseudo-bulges versus classical bulges. The utility of using D_n4000 – $\Delta\Sigma_1$ to study λ_{R_c} reinforces the notion that galaxy kinematics correlate both with structure and with stellar-population state, and indicates the importance of a multidimensional description for understanding bulge and galaxy evolution.

Key words: galaxies: bulges – galaxies: evolution – galaxies: formation – galaxies: fundamental parameters – galaxies: kinematics and dynamics – galaxies: structure.

1 INTRODUCTION

The rotational support of the stellar system in galaxies measures the relative magnitude of regular rotation to dispersion and shows important hints on galaxy evolution. The rotational support not only correlates with the galaxy specific angular momentum (Cortese et al. 2016), which is believed to determine the galaxy mass–size relation (Mo, Mao & White 1998; Shen et al. 2003), but also observationally correlates with bulge-building processes, the transformation of mass profiles from exponential to de Vaucouleurs shape, and, ultimately, quenching (Cappellari 2016; Graham et al. 2018).

With the advent of integral-field spectroscopic (IFS) surveys (e.g. Bacon et al. 2001; de Zeeuw et al. 2002; Cappellari et al. 2011; Croom et al. 2012; Sánchez et al. 2012; Bundy et al. 2014), an integrated parameter, λ_{R_c} , has been invented to quantify rotational support and has proven to be powerful in characterizing galaxy spatial kinematics (e.g. Emsellem et al. 2007; Cortese et al. 2016). To understand the connection between structure, stellar population, and kinematics, the correlations of λ_{R_c} with various properties have been widely investigated. The first attempt focused on early-type galaxies and revealed their inhomogeneity in kinematic structures (e.g. Emsellem et al. 2007; Krajnović et al. 2011; Cappellari 2016). Subsequent investigations expanded to a wider galaxy sample covering all morphological types. It was first shown with CALIFA galaxies (Sánchez et al. 2012) that

* E-mail: xiaohanw78@gmail.com (XW); yluo42@ucsc.edu (YL)

λ_{R_e} decreases with morphologies changing from spiral galaxies to elliptical galaxies (Querejeta et al. 2015; Falcón-Barroso et al. 2019). This morphology–kinematics correlation was further validated by SAMI (Sydney-AAO Multi-object Integral field spectrograph, Croom et al. 2012, 2021) and MaNGA (Mapping Nearby Galaxies at Apache Observatory, Bundy et al. 2014; Graham et al. 2018).

Morphology quantified by *Hubble* type is an approximate description of galaxy structure. The quantitative descriptions of galaxy structure, including Sérsic index, concentration (R_{90}/R_{50}), bulge-to-total ratio (B/T), and galaxy central density, help to characterize the galaxy mass distribution more accurately and reveal the complexity within each *Hubble* type. The studies with quantitative structural parameters show consistent results, that λ_{R_e} tends to decrease with increasing concentration, Sérsic index, and B/T (e.g. Querejeta et al. 2015; Cortese et al. 2016, 2022; Falcón-Barroso et al. 2019; Croom et al. 2021). The correlation of λ_{R_e} and galaxy mass distribution suggests that the change in λ_{R_e} is related to galaxy structural evolution, especially the growth of a dispersion-supported bulge. A recent study that performed kinematic bulge–disc decomposition for SAMI galaxies suggests that the λ_{R_e} of the galaxy can be fully explained by a combination of a dispersion-supported bulge and a rotation-supported disc (Oh et al. 2020).

Another possible factor that correlates with galaxy kinematics is galaxy stellar population. Observations of late-type galaxies have found that the discy structures tend to have younger stellar populations than bulges and stellar haloes (Lee et al. 2011; Sharma et al. 2014; González Delgado et al. 2015; Goddard et al. 2017). Therefore, the star formation history of a galaxy may influence the observed $\lambda_{R_e, \text{Star}}$ values. Moreover, violent processes including mergers can dramatically change stellar orbits, decrease rotational support, and may lead to galaxy quenching (Toomre 1977; Hernquist 1992; Naab, Khochfar & Burkert 2006). A detailed view of how galaxy λ_{R_e} correlates with galaxy stellar age for a sample covering all morphological types is given by van de Sande et al. (2018). They show that for both early- and late-type galaxies, stellar population age tends to decrease with rotational support (V/σ , λ_{R_e}) and galaxy intrinsic ellipticity. This correlation was further investigated by Wang et al. (2020) and Fraser-McKelvie et al. (2021) who measured the distribution of stellar λ_{R_e} on and below the galaxy star formation main sequence (SFMS). They found that galaxies on the SFMS are always fast rotators, while below the SFMS galaxies there is a sharp decrease of λ_{R_e} at the high-mass end, which they interpreted as being caused by multiple mergers for massive galaxies (Wang et al. 2020).

The two factors that correlate with kinematics, structural evolution and stellar population, are themselves correlated to some extent. Under the hierarchical clustering model where galaxies grow by mergers, the B/T ratio is expected to increase with stellar mass and stellar population age (e.g. White & Rees 1978; Cole et al. 1994; Baugh 2006). This phenomenon has been seen in both observations and simulations (e.g. Kauffmann et al. 2003b; Weinzirl et al. 2009; Hopkins et al. 2010; Bluck et al. 2014). Another scenario linking structural evolution and quenching is that a massive bulge can stabilize the galaxy and prevent further star formation (Martig et al. 2009). Therefore, a general correlation among structure, kinematics and stellar population is expected. The observations consistently show that, in a general way, all of the structural, stellar population, and kinematic properties correlate with one another and form a sequence. One end of the sequence is characterized by high random motions, older stellar populations, and higher B/T ratios. The other end of the sequence is characterized by high rotational support, active star formation, younger stellar populations, and lower B/T ratios (e.g.

Kormendy & Kennicutt 2004; Fisher 2006; Fisher & Drory 2008, 2010; Gadotti 2009; Fabricius et al. 2012; Fisher & Drory 2016; Falcón-Barroso et al. 2019; Croom et al. 2021). An illustration of the sequence can be seen in Croom et al. (2021), which shows a simultaneous decline in $\lambda_{R_e, \text{Star}}$ with increasing concentration and declining specific star formation rate for non-elliptical galaxies. A theoretical interpretation summarizing the kinematic and structural evolution for galaxies on and below the SFMS can be found in Wang et al. (2020).

However, all of the correlations along the sequence show considerable scatter. The inconsistency can be seen from high values of Sérsic index and B/T on the SFMS (Wuyts et al. 2011; Morselli et al. 2017), indicating that star-forming galaxies can have highly concentrated mass distributions. The inconsistency was further investigated under the effort to find the best structural predictor of galaxy quenching, which uncovers that structures and stellar populations evolve at different rates as galaxies begin to quench. Cheung et al. (2012) introduced the quantity Σ_1 , which is the projected stellar density within 1 kpc radius. They showed that Σ_1 was the best predictor of quenching among a variety of structural parameters measured for galaxies near $z \sim 1$. Fang et al. (2013) defined the quantity $\Delta\Sigma_1$ by subtracting the mass trend from Σ_1 and plotted $\Delta\Sigma_1$ versus global $\text{NUV} - r$ for a large sample of SDSS galaxies. The resulting figures showed an ‘elbow shape’ in which low $\Delta\Sigma_1$ galaxies were uniformly star-forming whereas high $\Delta\Sigma_1$ galaxies could be either star-forming or quenched (illustrated further in Fig. 2). Finally, Barro et al. (2017) and Lee et al. (2018) showed that the elbow pattern is present as early as $z \sim 3$, and thus this feature has been a fundamental property of galaxy evolution since very early times.

The relationship of structure to star formation was explored further by Luo et al. (2020) using various structural and stellar parameters for a large sample of SDSS galaxies. They reproduced the elbow patterns with $\Delta\Sigma_1$ and central D_n4000 (the 4000-Å break strength, stellar population age indicator). Luo et al. (2020) also compared $\Delta\Sigma_1$ with Gadotti’s (2009) bulge classification parameter $\Delta\mu_e$ from the Kormendy relation. The two parameters were found to agree well, making $\Delta\Sigma_1$ a good indicator of bulge structure. In summary, all of these works revealed the same trend in which quenched galaxies always have high central densities, while star-forming galaxies can have a range of central surface densities. Said differently, low-relative-central-density galaxies are always star-forming while high-relative-central-density galaxies can have a range of star formation rates.

Adding kinematics to this picture adds additional scatter. On the one hand, galaxies below the SFMS consistently show high B/T or Sérsic indices (e.g. Wuyts et al. 2011; Morselli et al. 2017), but significantly different $\lambda_{R_e, \text{Star}}$ at the low/high-mass end (e.g. Wang et al. 2020). This difference was interpreted as resulting from different quenching mechanisms at low and high mass. Cortese et al. (2022) used Σ_1 to characterize galaxy concentration for purely passive galaxies but found no correlation between Σ_1 and λ_{R_e} for this sample at fixed mass. On the other hand, although galaxies on the SFMS are typically fast rotators, the scatter of λ_{R_e} is always considerable, even among star-forming galaxies (van de Sande et al. 2018; Falcón-Barroso et al. 2019; Wang et al. 2020; Fraser-McKelvie et al. 2021).

To summarize, galaxy stellar rotational support (λ_{R_e}) correlates broadly with structural and stellar population properties, but superimposed on those general relations are additional subtrends that seem to be controlled by other variables. This complexity is hardly surprising, as it has been clear for many years that galaxies populate a multidimensional manifold, with the result that virtually every

simple scaling law in two dimensions shows residuals that typically correlate with other parameters. With that as background, it is therefore natural to look at λ_{R_e} in the same way, that is, to map its behaviour in a higher dimensional space that spans both structure and stellar-population state. That exploration in detail will be the topic of a future paper, and here we take a first step by mapping λ_{R_e} in just two dimensions, using $\Delta\Sigma_1$ to encapsulate structural information and central/global values of D_n4000 to describe the stellar population. Because elliptical galaxies are heavily influenced by mergers (Springel, Di Matteo & Hernquist 2005; Kormendy et al. 2009; Naab, Johansson & Ostriker 2009) and satellite galaxies may be influenced by environmental factors (Peng et al. 2010), we focus on disc galaxies and central/isolated galaxies only in this paper. We use kinematic data from MaNGA (Bundy et al. 2014) to study how the rotational support parameter λ_{R_e} varies across the 2D landscape of D_n4000 versus $\Delta\Sigma_1$. The choice of D_n4000 and $\Delta\Sigma_1$ as coordinates proves fortunate: a new ‘J-shape’ pattern emerges whereby λ_{R_e} increases with central D_n4000 when $\Delta\Sigma_1$ is low but decreases with $\Delta\Sigma_1$ when $\Delta\Sigma_1$ is high. The trends for low- $\Delta\Sigma_1$ objects are especially clean and suggest a possible evolutionary path for these objects in star formation rate and λ_{R_e} versus stellar mass. Still other correlations, for kinematically and morphologically disturbed galaxies, are described along the way.

The paper is organized as follows. Section 2 describes the data and sample selection, introduces the parameters we computed, and discusses possible biases in the measurements. Section 3 presents our main finding of the J-shaped pattern in central D_n4000 versus $\Delta\Sigma_1$. In Section 4, we show how galaxy rotational support depends on stellar mass and central stellar population age for low- $\Delta\Sigma_1$ galaxies and offer a simple evolutionary scenario to account for the observed trends. In Section 5, we discuss possible evolutionary tracks on D_n4000_{centre} versus $\Delta\Sigma_1$ space and re-express our findings for λ_{R_e} in the language of pseudo-bulges and classical bulges. Section 6 summarizes our results and open issues. In this paper, we adopt a concordance lambda-cold dark matter cosmology: $H_0 = 70 \text{ km (s Mpc)}^{-1}$, $\Omega_M = 0.3$, and $\Omega_\Lambda = 0.7$.

2 DATA AND ANALYSIS

2.1 MaNGA IFU observations

The MaNGA Survey provides spatially resolved spectra and property maps for ~ 10000 galaxies in the local universe ($z < 0.15$, Bundy et al. 2014). It utilizes the 2.5-m Sloan Foundation Telescope in its spectroscopic mode (Gunn et al. 2006) and the two dual channel BOSS spectrographs (Smee et al. 2013), which cover a wavelength range of $3600 - 10300 \text{ \AA}$ with $R \sim 2000$ and spatial resolution of $\sim 2.5 \text{ arcsec}$ (Bundy et al. 2014). The instrumental details are described in Drory et al. (2015). Galaxies in this paper are selected from MaNGA Project Launch-11 (MPL-11), the latest and most complete version of MaNGA. Data used in this paper are from the SPX MAPS provided by the MaNGA Data Analysis Pipeline (DAP, Belfiore et al. 2019; Westfall et al. 2019), which makes use of PPXF (Cappellari & Emsellem 2004; Cappellari 2017) to process spectra and produce 2D maps of properties.

2.2 Photometric and spectroscopic measurements

For sample selection and kinematic measurements, we adopt elliptical Petrosian effective radii from the extended NASA–Sloan Atlas (NSA) catalogue (Blanton et al. 2011; Wake et al. 2017), galaxy axis ratio b/a from Simard et al.’s (2011) catalogue, and stellar mass from

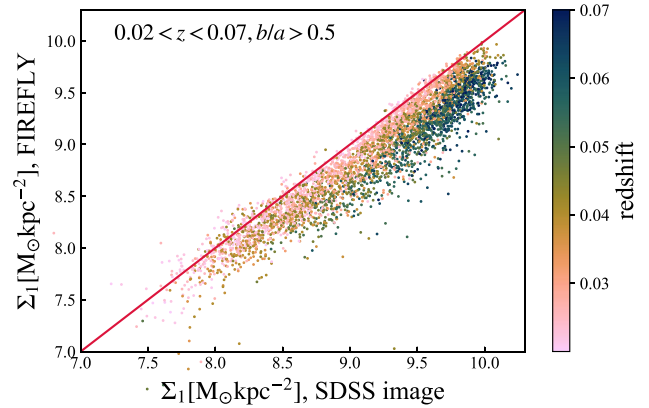


Figure 1. Σ_1 calculated by MaNGA mass maps generated by FIREFLY versus Σ_1 calculated by colour difference in SDSS images, coloured by redshift. The sample is limited to $0.02 < z < 0.07$ and $b/a > 0.5$ (see sample selection in Section 2.3). The $\Sigma_{1, \text{MaNGA}}$ is systematically lower than $\Sigma_{1, \text{SDSS}}$, and the difference increases with redshift, consistent with the spatial resolution difference of MaNGA and SDSS. We use SDSS measurements in our analysis.

MPA-JHU DR7 value-added catalogue (Kauffmann et al. 2003a). The choice of elliptical Petrosian R_e is consistent with MaNGA target selection (Wake et al. 2017), as NSA’s single Sérsic R_e tends to be systematically overestimated for galaxies with higher Sérsic indices (Simard et al. 2011; Wake et al. 2017).

We also adopt the smoothness parameter $S2$ from Simard et al. (2011). The smoothness parameter $S2$ is defined in Simard et al. (2009), calculated as a sum of fractional total light and asymmetry light of image residuals from a smooth symmetric model, and therefore is an indicator of galaxy asymmetry and clumpiness (Schade et al. 1995; Simard et al. 2002). A higher $S2$ indicates higher asymmetry or higher clumpiness. We adopt $S2_g$, which is calculated with the g -band SDSS images. The choice of band for $S2$ does not have a large effect on our results.

The central density is quantified by $\Delta\Sigma_1$, the residual of Σ_1 to stellar mass, as defined in Luo et al. (2020). Σ_1 , the stellar surface mass density within the radius of 1 kpc, is measured with i -band luminosities of SDSS DR7 images (Abazajian et al. 2009) and i -band mass-to-light ratios from Fang et al. (2013). $\Delta\Sigma_1$ is calculated by a function which separates the two density peaks in Σ_1 at fixed stellar mass (Luo et al. 2020):

$$\Delta\Sigma_1 = \log \Sigma_1 + 0.275(\log M_*)^2 - 6.445 \log M_* + 28.059. \quad (1)$$

The spatial resolution for SDSS ($\sim 1.5 \text{ arcsec}$) is better than MaNGA ($\sim 2.5 \text{ arcsec}$), and the luminosity profiles of SDSS images are seeing-corrected for Σ_1 measurements (Zhao et al., in preparation). Therefore, we choose to adopt Σ_1 calculated from SDSS DR7 images instead of recalculating it with data from MaNGA. Fig. 1 compares Σ_1 from SDSS images with Σ_1 calculated by the mass maps provided by MaNGA FIREFLY value-added catalogue (Neumann et al. 2022), coloured by redshift. As expected by the difference of spatial resolution, $\Sigma_{1, \text{FIREFLY}}$ is systematically smaller than $\Sigma_{1, \text{SDSS}}$, and the offset increases with redshift.

The stellar populations of galaxies are characterized by the 4000- \AA break strength, D_n4000 . In this paper, we calculate mean D_n4000 in radii of 1.5 arcsec (SDSS fibre size) and bundle size (MaNGA field of view) from MaNGA maps, weighted by SPECINDEX_WGT (flux of linear continuum, see section 5.2.2 in Westfall et al. 2019; Abdurro’uf et al. 2022) provided in MaNGA DAP. Fibre measurements are

Table 1. Sample selection descriptions.

Criteria	N
$0.02 < z < 0.07$	7735
$0.5 < b/a < 0.85$	3270
Isolated or central	2170
Disc galaxies	1671
Merging probability < 0.2	1589
$M_* > 10^{9.5} M_\odot$	1347
$R_e > 5$ arcsec, IFU size $> 1.2R_e$	666
esweight > 0	649
Checked by eye for good inclination	584
Good data quality	533
No misalignment between photometry and kinematics	484

denoted as ‘centre’, while bundle measurements are denoted as ‘global’. These labels represent that these measurements serve as indicators of the central and the overall stellar population ages. The choice of the bundle size ensures that the global measurements are effectively averaged across the entire galaxy. We checked the results by using $D_n4000_{R_e}$ as indicators of global stellar population ages and found that the main conclusions are not affected.

2.3 Galaxy sample

2.3.1 Main sample selection

We reiterate here that our goal is to study well-resolved galaxies with substantial disc components. With that in mind, we set the following requirements, which are summarized in Table 1:

- (i) Galaxies are limited to $0.02 < z < 0.07$.

Nearby galaxies ($z < 0.02$) are rejected as their intrinsic proper motions can affect distance measurements. Galaxies are restricted to $z < 0.07$ to mitigate the seeing effect for Σ_1 , as when $z > 0.07$, the apparent size of 1 kpc will be smaller than 0.7 arcsec, which is half of seeing for SDSS images (Fang et al. 2013; Luo et al. 2020).

- (ii) Galaxies are limited to have stellar mass higher than $10^{9.5} M_\odot$. In Luo et al. (2020), only galaxies with mass higher than $10^{9.5} M_\odot$ are fitted to obtain the $\Delta\Sigma_1$ function.

- (iii) Only isolated or central disc galaxies are included.

Satellite galaxies can be affected by their environmental effects. In this paper, we only focus on isolated or central galaxies. Satellite galaxies are excluded by group designation ($M_{\text{rank}} > 1$) from Yang et al. (2012).

The morphology classification is from Galaxy Zoo 1 (Lintott et al. 2011) and we exclude galaxies with the value of ELLIPTICAL = 1. However, the visual classification may not work well and may result in losing disc galaxies. We checked the classification for the whole MaNGA sample and found some of the galaxies with ELLIPTICAL = 1 show low Sérsic indices, which are possible lost disc galaxies. Nevertheless, the galaxies with ELLIPTICAL = 1 and Sérsic indices < 2 cover only a small fraction (0.7 per cent) compared to galaxies with ELLIPTICAL = 0. Therefore, we simply adopt the classification based on ELLIPTICAL = 1.

- (iv) The probability of merging (P_{MG} , from Galaxy Zoo 1; Lintott et al. 2011) is lower than 0.2.

- (v) Axis ratio b/a is from 0.5 to 0.85.

The axis ratio is required to be larger than 0.5 to exclude near edge-on galaxies, where Σ_1 can be overestimated by disc component contamination or reduced by dust obscuration. The axis ratio is required to be smaller than 0.85 to reject nearly face-on galaxies whose inclination corrections are not reliable. We make inclination

correction for velocity, but measurements of b/a for nearly face-on galaxies may be not accurate and the error of correction can be severe. We made a test with a limited sample of $0.5 < b/a < 0.7$ and the main results do not change. In addition, the b/a measurements, adopted for inclination correction, may not well represent the true inclination angle due to non-zero disc height and can be biased by structures like bars and asymmetric spiral arms. We checked the sample by eye and rejected all edge-on galaxies and apparently face-on galaxies remaining after the b/a cut.

- (vi) The effective radius is larger than 5 arcsec, and the galaxy is covered to at least $1.2R_e$ by the MaNGA bundle.

Beam smearing effects can cause λ_{R_e} to be underestimated. By requiring $R_e > 5$ arcsec, we select galaxies sampled by at least four beams along their major axes, such that their kinematics are better resolved. Simulations, discussed in Appendix B, indicate that beam-smearing effects on λ_{R_e} are small for galaxies larger than 5 arcsec. We also require galaxies to be covered to $1.2R_e$ to obtain accurate and reliable measurements within R_e . This allows us to avoid spaxels near the edge of the IFU field of view, which may suffer from low signal-to-noise ratio (S/N) and unreliable kinematics.

- (vii) No galaxies with ‘bad quality’.

Spaxels flagged by the MaNGA DRP as DONOTUSE or FORESTAR, or with SNR < 3 are masked in our analysis. The flag of DONOTUSE, however, varies with properties for the same spaxel, and we make our selection based on kinematic measurements. We exclude galaxies whose fraction of rejected spaxels within $1 R_e$ ellipse is larger than 10 per cent.

- (viii) The misalignment between the photometry and kinematic major axes must be $< 30^\circ$.

Due to the effect of bars, the major axis of photometry may be misaligned with the kinematic major axis. As we adopt photometric R_e and b/a for kinematic measurements, we calculate kinematic major axis position angles for stellar velocity fields using `fit_kinematic_pa`,¹ and exclude galaxies whose misalignment between photometry and kinematic major axes is larger than 30° .

The above cuts yield a sample of 484 galaxies. The resulting sample sizes under each criterion are summarized in Table 1.

The distribution of the sample on $D_n4000_{\text{centre}} - \Delta\Sigma_1$ is shown in Fig. 2. The distribution shows the classic elbow shape, where galaxies with low $\Delta\Sigma_1$ are always strongly star-forming but galaxies with high $\Delta\Sigma_1$ cover a large range of star formation rate. The distributions in both x - and y -axes are bimodal. Their minima, $\Delta\Sigma_1 = 0$ and $D_n4000_{\text{centre}} = 1.66$ (a rough ridgeline for green valley), can be used to define four quadrants for future reference: centrally star-forming galaxies with high $\Delta\Sigma_1$, centrally star-forming galaxies with low $\Delta\Sigma_1$, centrally quiescent galaxies with high $\Delta\Sigma_1$, and centrally quiescent galaxies with low $\Delta\Sigma_1$. The last type only contains few galaxies and is not discussed in this paper. This classification is consistent with Luo et al. (2020) who uses $\Delta\Sigma_1 = 0$ as a classification boundary.

Fig. 3 shows the distributions of the three main types of galaxies on $\Sigma_1 - M_*$, SSFR $- M_*$, and $R_{50} - M_*$, with background of SDSS sample (Luo et al. 2020). An important feature is that galaxies with low $\Delta\Sigma_1$ always have larger radii than galaxies with high $\Delta\Sigma_1$ at a fixed mass. This feature will be further discussed in Section 5.

The data points in Fig. 2 are weighted to correct the sample to be volume-limited. We adopt a method like that of Fraser-McKelvie & Cortese (2022), by calculating the ‘sampling rate’ of our sample,

¹<http://purl.org/cappellari/software>

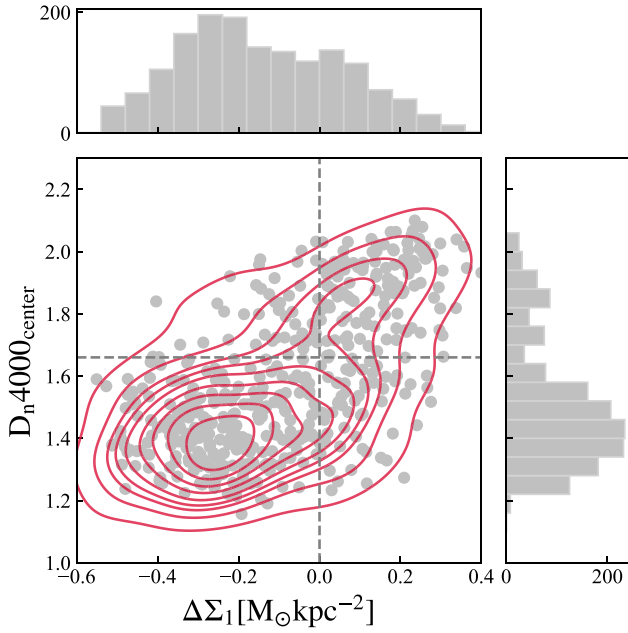


Figure 2. $D_{n,4000,\text{centre}}$ versus $\Delta\Sigma_1$ and their histograms, showing how the ‘elbow pattern’ studied by Fang et al. (2013) and Luo et al. (2020) is revealed in this sample. The subscript ‘centre’ means the parameter is measured within a 1.5 arcsec radius to match the SDSS fibre, same in the following text. The crimson curves represent weighted number density contours, where the points are weighted by esweight divided by the sampling fraction (see the text), to correct the sample into a volume-limited sample. The vertical dashed line $\Delta\Sigma_1 = 0$ is the classification boundary of bulge types in Luo et al. (2020). The horizontal grey dashed line $D_{n,4000,\text{centre}} = 1.66$ is a rough indicator of green valley. In this way, galaxies are divided into four bins, centrally star-forming galaxies with high $\Delta\Sigma_1$ (lower right), centrally star-forming galaxies with low $\Delta\Sigma_1$ (lower left), centrally quiescent galaxies with high $\Delta\Sigma_1$ (upper right), and centrally quiescent galaxies with low $\Delta\Sigma_1$ (upper left).

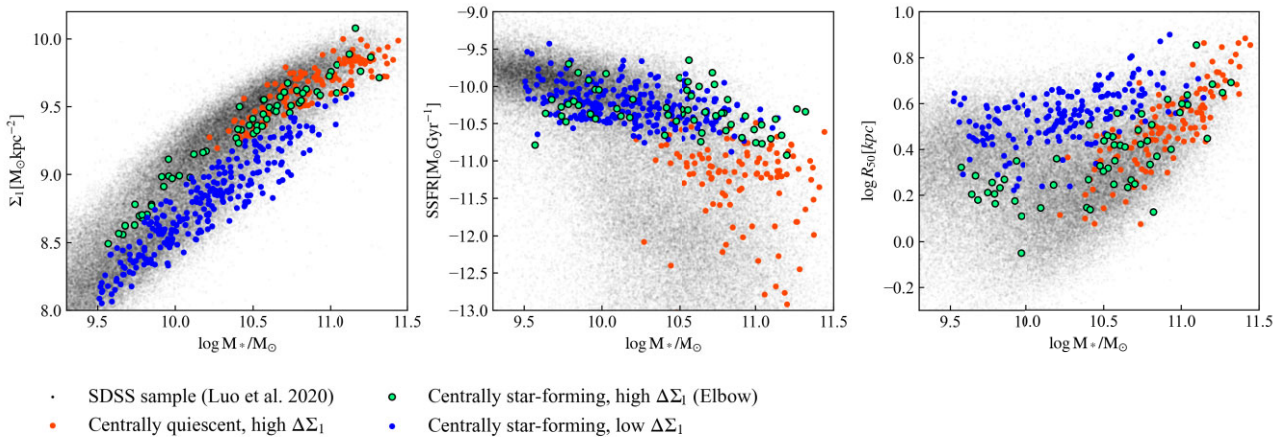


Figure 3. From left to right are Σ_1 versus stellar mass, specific star formation rate versus stellar mass, and half-mass radius versus stellar mass. The grey points in the background are SDSS sample with $0.02 < z < 0.07$ and $b/a > 0.5$. The red points are centrally quiescent high- $\Delta\Sigma_1$ galaxies ($\Delta\Sigma_1 > 0$ and $D_{n,4000,\text{centre}} > 1.66$) in our sample, the green open circles are elbow galaxies ($\Delta\Sigma_1 > 0$ and $D_{n,4000,\text{centre}} < 1.66$), and the blue points are centrally star-forming low- $\Delta\Sigma_1$ galaxies ($\Delta\Sigma_1 < 0$ and $D_{n,4000,\text{centre}} < 1.66$). The left two figures represent the definitions of the three subsets. Specifically, low- $\Delta\Sigma_1$ galaxies have lower central density and tend to be star-forming, while high- $\Delta\Sigma_1$ galaxies have higher central density and cover a large range of star formation. As shown in the third figure, low- $\Delta\Sigma_1$ galaxies always have larger radii than high- $\Delta\Sigma_1$ galaxies at fixed mass. This size difference is consistent with the central densities. This size difference also sheds light on bulge evolution, which is discussed in Section 5.

which is the fraction of selected galaxies to a MaNGA parent sample ($0.02 < z < 0.07$, $\log M_*/M_\odot > 9.5$, and $\text{esweight} > 0$) in bins of $M_* - z$. We then weight each galaxy by esweight (provided by MaNGA, see Wake et al. 2017) divided by the number fraction. This correction is applied for the density plot (Fig. 2) and when calculating correlation coefficients (Figs 7 and 8). We clarify that the correction cannot fully avoid the bias introduced by the requirement of effective radii ($R_e > 5$ arcsec), and the sample is biased to larger galaxies. Discussion about this bias is in Section 5.3 and will be further addressed in a future work (Wang et al. in preparation).

2.3.2 Clean sample and subsamples

Galaxy kinematics may be affected by disturbances. External disturbances, including mergers, interactions and gas infall, may result in asymmetric or irregular morphologies and alter stellar orbits. Internal disturbances, often associated with bars, can also change the orbits and may heat the stars. To investigate the effects of disturbance on galaxy kinematics, we define three subsets, ‘disturbed morphology’, ‘perturbed kinematics’, and ‘clean sample’, from the main sample.

To select the galaxies with disturbed morphologies, we set $S2_g > 0.17$, which is the median value of the main sample, as a preliminary selection, and further update the selection by checking galaxy images. We flag the galaxies with relatively irregular or asymmetric morphologies with ‘disturbed morphology’, which are possible to have experienced mergers or interactions. Examples of such objects are shown in Fig. F1. Then, we check the velocity maps for all galaxies in our sample, and flag the galaxies with twisted central velocity maps as ‘perturbed kinematics’. Most often such disturbances are associated with bars. Notice that the two subsets of ‘disturbed morphology’ and ‘perturbed kinematics’ are not mutually exclusive; they have an intersection of 13 galaxies. Finally, based on these analyses, we define the clean sample as those galaxies not flagged as having either ‘disturbed morphology’ or ‘perturbed kinematics’. We return to these peculiar subsets again in Section 4. The criteria and numbers of each subset are shown in Table 2.

Table 2. Description of subsamples.

Description	Criteria	N
Disturbed morphology	Irregular or asymmetric morphology	33
Perturbed kinematics	Centrally twisted velocity maps	232
Clean sample	Settled discs, regular morphology, and kinematics	232

2.4 Proxy for rotation support: λ_{R_e}

We use λ_{R_e} as the galaxy rotational support indicator. λ_{R_e} is a dimensionless proxy for observed projected specific angular momentum, defined in Emsellem et al. (2007). The definition of λ_{R_e} via 2D spectroscopy is

$$\lambda_R = \frac{\sum_{i=1}^N F_i R_i |V_i|}{\sum_{i=1}^N F_i R_i \sqrt{V_i^2 + \sigma_i^2}}, \quad (2)$$

where F_i , R_i , V_i , and σ_i are the flux, projected circular radius, velocity, and velocity dispersion of the i th spatial bin (Emsellem et al. 2007). In the original definitions of λ_{R_e} in Emsellem et al. (2007), V_i and σ_i represent projected line-of-sight kinematics. However, it is possible to make proper inclination correction for velocity of disc galaxies. We correct V to be $V/\sin i$, and assume that σ is isotropic and does not need correction. Therefore, kinematic measurements in this paper are deprojected. The parameter $\sin i$ is calculated by:

$$\sin^2 i = \frac{1 - (b/a)^2}{1 - \alpha^2}, \quad (3)$$

where α is the ratio of disc scale height over disc scale length and b/a is the axis ratio. This formula is based on the oblate model and from Holmberg (1958). The value of α is observed to range from 0.1 to 0.3 for local galaxies (Padilla & Strauss 2008; Unterborn & Ryden 2008; Rodríguez & Padilla 2013). We adopt a typical value of 0.2 and apply it to all galaxies in our sample. λ_{R_e} is calculated in ellipses with kinematic major axis, photometric axis ratio, and Petrosian R_e .

λ_{R_e} may be underestimated due to the beam smearing effect. Empirical corrections for beam smearing effect on λ_{R_e} have been developed (Graham et al. 2018; Harborne et al. 2020). However, the correction method is tested with observation data for early-type galaxies only (Graham et al. 2018), which are not covered in this work. Therefore, we choose to not apply any beam smearing correction for λ_{R_e} in this paper. To estimate the effect of beam smearing effect, we have made a simulation, which is similar to the method in Greene et al. (2018). We have found that, for galaxies with R_e larger than 5 arcsec, the beam smearing effect is not significant and does not bias our results. Details of the simulation are in Appendix B. The beam smearing correction will be explored for a wider range of galaxies in future work (Wang et al. in preparation).

In our analysis, dispersions are corrected for instrumental resolution with σ_{corr} provided by the MaNGA DAP. However, a problem arises for regions with low dispersion, where errors in observations can result in imaginary values of the corrected dispersion. Ignoring such pixels can lead to biased overestimation of dispersion values. It is recommended in Westfall et al. (2019) to retain these negative σ^2 values, and we keep these values and utilize a luminosity-weighted mean-squared dispersion to account for their contributions. This approach ensures a more accurate representation of the dispersion properties in our analysis.

3 ROTATIONAL SUPPORT AS A FUNCTION OF RELATIVE CENTRAL DENSITY AND STELLAR POPULATION

In this section, we present how galaxy rotational support, indicated by λ_{R_e} , varies as a function of stellar population (D_n4000) and relative central density ($\Delta\Sigma_1$).

Fig. 4 shows the distribution of $\lambda_{R_e, \text{Star}}$ in the $D_n4000_{\text{global}} - \Delta\Sigma_1$ and $D_n4000_{\text{centre}} - \Delta\Sigma_1$ spaces. Colours in the right panels are smoothed by the LOESS method² (Cappellari et al. 2013), an implementation of 2D Locally Weighted Regression (Cleveland & Devlin 1988), to get a view of the average distribution. We mark globally quenched galaxies ($D_n4000_{\text{global}} > 1.8$) as crosses and galaxies in the green valley ($1.6 < D_n4000_{\text{global}} < 1.8$) as edged circles, to better trace their locations when central D_n4000 is used.

The most intriguing feature in Fig. 4 is the smoothly varying colour pattern in both global and central parameter spaces. For global $D_n4000 - \Delta\Sigma_1$ (top row), the distribution of $\lambda_{R_e, \text{Star}}$ follows tilted stripes, where $\lambda_{R_e, \text{Star}}$ increases first with global D_n4000 when star forming, and then decreases as galaxies enter the green valley and quench. The stripes are almost horizontal when $\Delta\Sigma_1$ is negative, where $\lambda_{R_e, \text{Star}}$ is weakly dependent on $\Delta\Sigma_1$, and get tilted where $\lambda_{R_e, \text{Star}}$ decreases with both $\Delta\Sigma_1$ and global D_n4000 when $\Delta\Sigma_1$ is high. This pattern of horizontal and tilted stripes can be described as a ‘fainted J-shape’, where $\lambda_{R_e, \text{Star}}$ increases with global D_n4000 when $\Delta\Sigma_1$ is low, and decreases with both $\Delta\Sigma_1$ and global D_n4000 when $\Delta\Sigma_1$ is high. The ‘J-shape’ pattern is more prominent for central $D_n4000 - \Delta\Sigma_1$ in the bottom row, where the colour stripes are almost horizontal for negative $\Delta\Sigma_1$ and get vertical for positive $\Delta\Sigma_1$. $\lambda_{R_e, \text{Star}}$ increases with central D_n4000 when $\Delta\Sigma_1$ is low, and decreases with $\Delta\Sigma_1$ when $\Delta\Sigma_1$ is high.

For both global and central parameter spaces, the ‘dominant’ parameter that correlates best with $\lambda_{R_e, \text{Star}}$ changes with the locations in the space, with a transition at almost $\Delta\Sigma_1 \sim 0$. When $\Delta\Sigma_1$ is high, $\lambda_{R_e, \text{Star}}$ tends to decrease with both D_n4000_{global} and $\Delta\Sigma_1$ with a tilted pattern, but shows almost no correlation with central D_n4000 . This is possibly owing to the intermixing of the green valley and globally quenched objects when central D_n4000 is used. In retrospect, the complexity at high $\Delta\Sigma_1$ is not unexpected, as galaxies with high $\Delta\Sigma_1$ show a wide range of star formation rates (e.g. Fang et al. 2013; Luo et al. 2020). By contrast, galaxies with low $\Delta\Sigma_1$ are more homogeneous with a narrower range of D_n4000 , and are found to have similar behaviour in both parameter spaces, where $\lambda_{R_e, \text{Star}}$ tends to increase with both central and global D_n4000 , with only a quite weak dependence on $\Delta\Sigma_1$. This trend is opposite to the general trend mentioned in the Introduction that $\lambda_{R_e, \text{Star}}$ tends to decrease with increasing stellar population age. In particular, $\lambda_{R_e, \text{Star}}$ shows a tighter correlation with central D_n4000 than global D_n4000 . This is shown by the fact that the low- $\Delta\Sigma_1$ galaxies with different $\lambda_{R_e, \text{Star}}$ are closely mixed in global D_n4000 but more widely spread out in central D_n4000 . In other words, central D_n4000 is a better predictor for $\lambda_{R_e, \text{Star}}$, which is measured within $1 R_e$. This correlation between central stellar population and global kinematics, that is opposite to the general relation, will be further investigated in the next section.

It is natural to ask whether the above patterns are actually mass-effect patterns. To investigate this, we divide the sample into four mass bins and show their distributions separately in Fig. 5. The first impression from Fig. 5 is the bulk movement of populations in the diagram with stellar mass. The galaxy population slowly moves from

²<http://purl.org/cappellari/software>

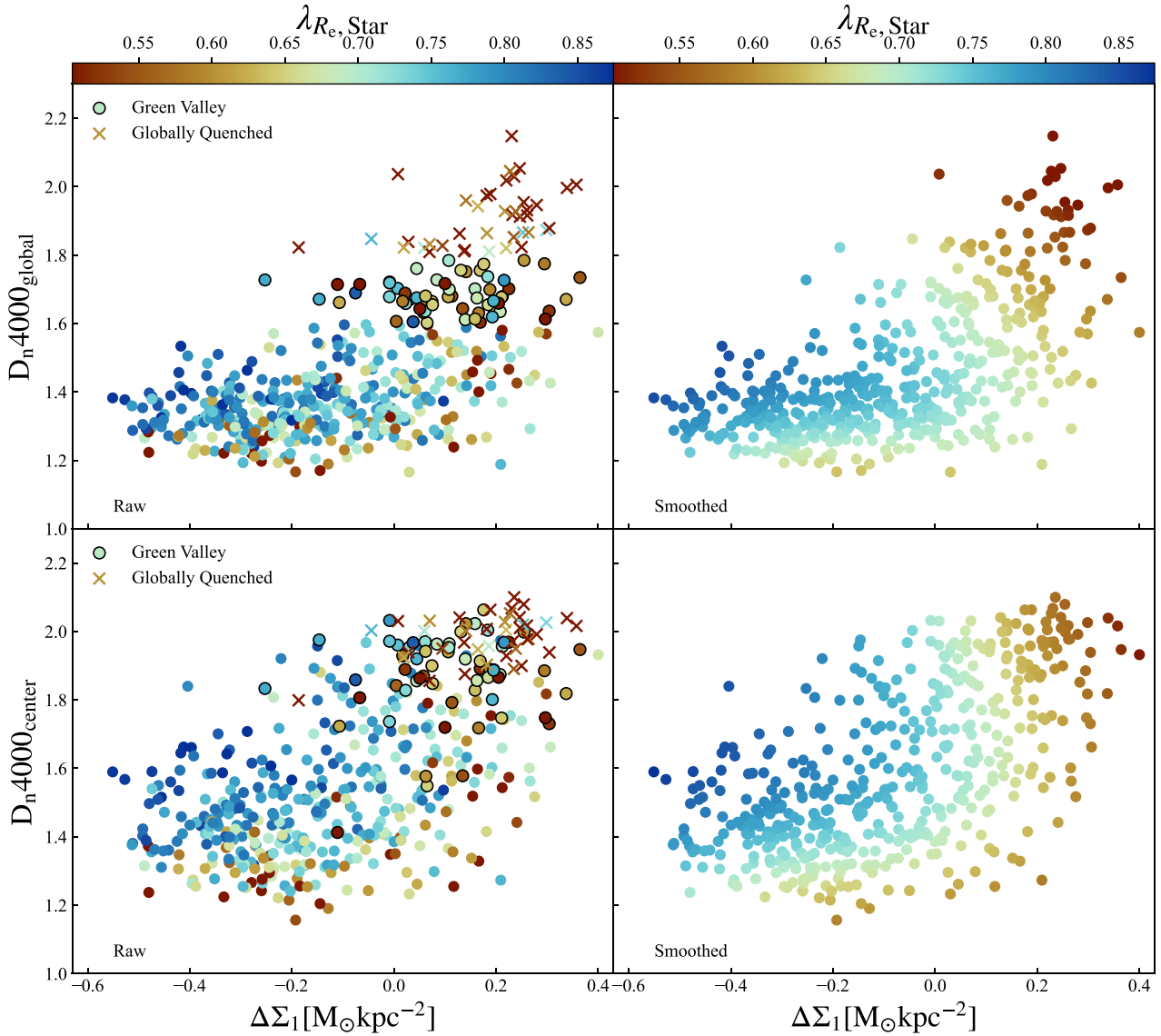


Figure 4. D_n4000_{global} and D_n4000_{centre} versus $\Delta\Sigma_1$ coloured by $\lambda_{R_e, \text{Star}}$. The left column shows the original scatter plots and the right panels are LOESS smoothed plots. Fully quenched galaxies ($D_n4000_{\text{global}} > 1.8$) are labelled as cross markers and galaxies in green valley ($1.6 < D_n4000_{\text{global}} < 1.8$) are circles with black edges. The distribution of $\lambda_{R_e, \text{Star}}$ on D_n4000_{global} versus $\Delta\Sigma_1$ space shows a non-monotonic tilted pattern, where $\lambda_{R_e, \text{Star}}$ first increases and then decreases with D_n4000_{global} . The distribution of λ_{R_e} on central D_n4000 versus $\Delta\Sigma_1$ is ‘J-shaped’, in which λ_{R_e} increases as D_n4000_{centre} increases for when $\Delta\Sigma_1$ is low, and decreases as $\Delta\Sigma_1$ increases when $\Delta\Sigma_1$ is high.

lower left to upper right, with $\Delta\Sigma_1$ and D_n4000 both increasing, as stellar mass increases. This is consistent with the general trend that $\lambda_{R_e, \text{Star}}$ tends to decrease with D_n4000 and $\Delta\Sigma_1$, as the data move from the horizontal arm (dominated by high $\lambda_{R_e, \text{Star}}$) to the vertical arm (dominated by low $\lambda_{R_e, \text{Star}}$) of the elbow distribution. Therefore, stellar mass does play a role in determining the shape of the overall distribution and the general relations. However, the colour distributions are not simply caused by mass effect, as shown by the fact that the elbow distribution is present separately in the two middle mass bins and by the fact that the horizontal and vertical colour patterns are each individually visible over a wide range of mass.

The new ‘J-shaped’ pattern reproduces the familiar trends that $\lambda_{R_e, \text{Star}}$ tends to decrease with D_n4000 and $\Delta\Sigma_1$, but reveals a more complex pattern underlying both trends. In addition to the large-

scale trends, it has also been found that stellar rotational support increases first and then decreases with stellar population age (Falcón-Barroso et al. 2019; Croom et al. 2021), consistent with what is shown by the J-shape pattern. Furthermore, investigations on $\lambda_{R_e, \text{Star}}$ and galaxy structure found that $\lambda_{R_e, \text{Star}}$ has a weak dependence on R_{90}/R_{50} with a relatively flat slope when R_{90}/R_{50} is low (Falcón-Barroso et al. 2019; Croom et al. 2021), consistent with the relatively horizontal colour patterns in Fig. 4 when $\Delta\Sigma_1$ is low. Investigations utilizing $\Delta\Sigma_1$ show that $\lambda_{R_e, \text{Star}}$ decreases with $\Delta\Sigma_1$ for star-forming galaxies but no trends for passive galaxies (Cortese et al. 2022). This finding also agrees with the colour distribution in each mass bin, as shown in the top panel of Fig. 5, which further specifies that introducing central/global stellar population can help reduce the scatter of $\lambda_{R_e, \text{Star}}$ versus $\Delta\Sigma_1$ for star-forming galaxies. In summary, the J-shape pattern is consistent with previous observations, and in

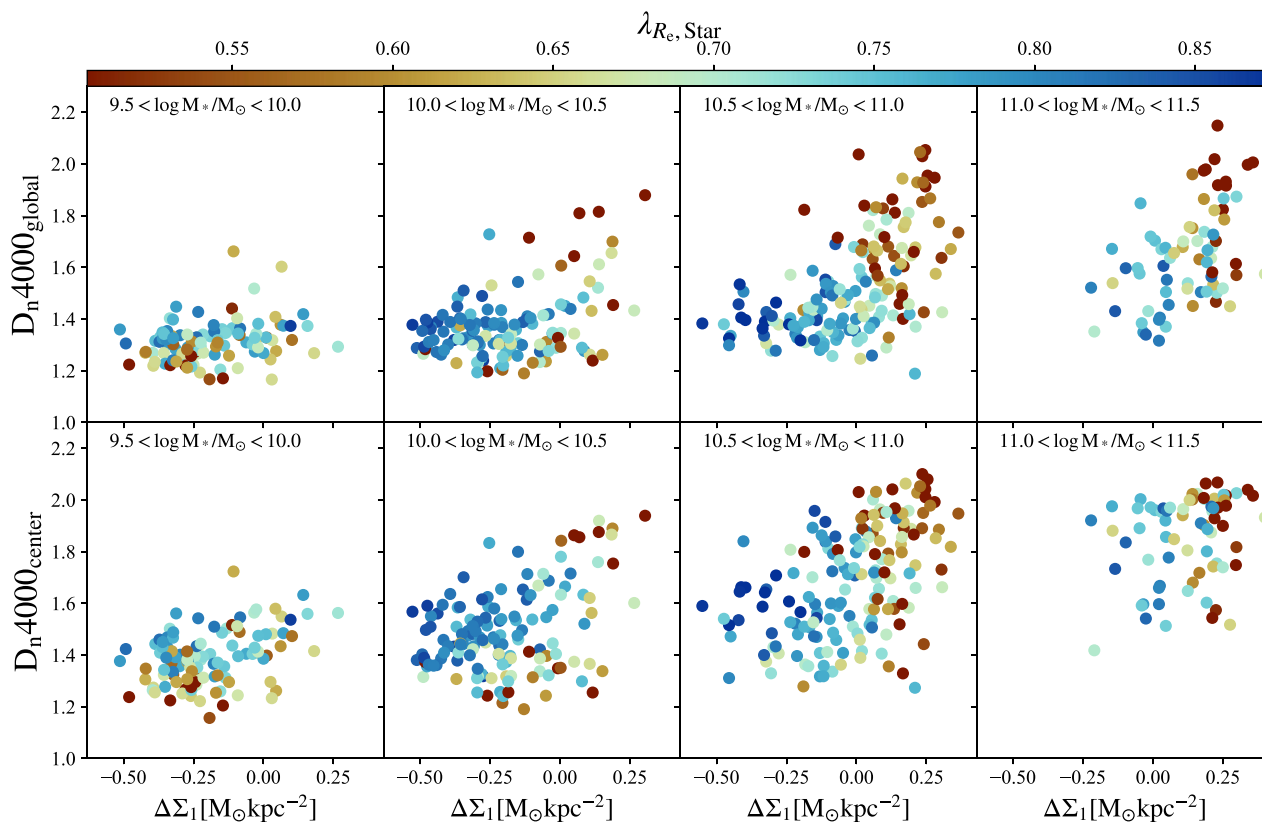


Figure 5. $\lambda_{R_e, \text{Star}}$ as a function of D_n4000 and $\Delta\Sigma_1$ in four mass bins. The top and bottom panels separately show D_n4000_{global} and D_n4000_{centre} versus $\Delta\Sigma_1$ coloured by $\lambda_{R_e, \text{Star}}$. As stellar mass increases, the whole population moves from lower left to higher right along the elbow-shaped distribution. The colour pattern gradually changes from horizontal to vertical, indicating the main dependence of kinematics changes from stellar population to structures (see the text).

particular uncovers the whole pattern and subtrends by utilizing a 2D coordinate that combines stellar population and structure.

4 POSSIBLE KINEMATIC EVOLUTION OF DISC GALAXIES WITH LOW RELATIVE CENTRAL SURFACE DENSITY

In this section, we focus on galaxies with low $\Delta\Sigma_1$, whose $\lambda_{R_e, \text{Star}}$ typically increase with D_n4000 , particularly for central stellar populations. This trend exists within each mass bin (the left three bins in Fig. 5), while $\lambda_{R_e, \text{Star}}$ also tends to increase with stellar mass on average, shown as the increasing fraction of deep blue points versus mass for low- $\Delta\Sigma_1$ galaxies in Fig. 5. To get a better view of how $\lambda_{R_e, \text{Star}}$, D_n4000_{centre} , and mass correlate with each other, we select the galaxies with negative $\Delta\Sigma_1$ and $D_n4000_{\text{centre}} < 1.66$ (252 galaxies), where the trend of $\lambda_{R_e, \text{Star}}$ versus D_n4000 is the clearest, and plot their distribution on $\lambda_{R_e, \text{Star}}$ versus mass, colouring the points by central D_n4000 . The results are shown in Fig. 6(a). A complementary view is shown in Fig. 6(b) of $\lambda_{R_e, \text{Star}}$ versus central D_n4000 with the points coloured by stellar mass.

Fig. 6 clearly indicates the aforementioned trends of increasing $\lambda_{R_e, \text{Star}}$ with stellar mass and D_n4000 , and increasing $\lambda_{R_e, \text{Star}}$ with central D_n4000 at a fixed stellar mass. A new feature revealed in Fig. 6 is that both distributions consist of a relatively tight ridgeline, along which $\lambda_{R_e, \text{Star}}$ increases with D_n4000_{centre} and stellar mass, accompanied by a fringe population of low $\lambda_{R_e, \text{Star}}$ ‘outliers’ lying below.

The relations of $\lambda_{R_e, \text{Star}}$ versus stellar mass and stellar population have been investigated in previous studies. Overall trends are that $\lambda_{R_e, \text{Star}}$ decreases with stellar mass (e.g. Brough et al. 2017; Veale et al. 2017; van de Sande et al. 2017; Greene et al. 2018) and stellar population age (e.g. van de Sande et al. 2018; Falc3n-Barroso et al. 2019; Wang et al. 2020; Fraser-McKelvie et al. 2021), but a closer reading reveals higher order complexities. For example, a decrease in $\lambda_{R_e, \text{Star}}$ at low stellar mass is visible in some samples (Falc3n-Barroso et al. 2019; van de Sande et al. 2021a, b), as well as a decrease in $\lambda_{R_e, \text{Star}}$ for highly star-forming galaxies, also at the low-mass end (Wang et al. 2020; Croom et al. 2021; Fraser-McKelvie et al. 2021). The results of Figs 4–6 together now show that these individual subtrends can be understood as parts of a larger, more complicated, but smoothly varying higher dimensional manifold. The general trend masks the existence of different and possibly opposite subtrends within the population, which we are dissecting here by isolating the subpopulation.

We now turn to the question of the formation channels of the ridgeline and the scattered outliers in Fig. 6. Since massive galaxies are further along the arc of star formation versus mass and have older stellar populations, the increasing trend of rotational support versus stellar mass may also contribute to the upward slope of $\lambda_{R_e, \text{Star}}$ versus D_n4000_{centre} in Fig. 6(b). That is, D_n4000_{centre} and rotational support may be evolving together with increasing stellar mass. This simple scenario is consistent with the increasing specific angular momentum of the accreted gas with time (Kassin et al. 2012; Simons et al. 2017; Renzini 2020), which makes galaxies spinup in discs as they assemble their mass by forming stars (Simons et al. 2017;

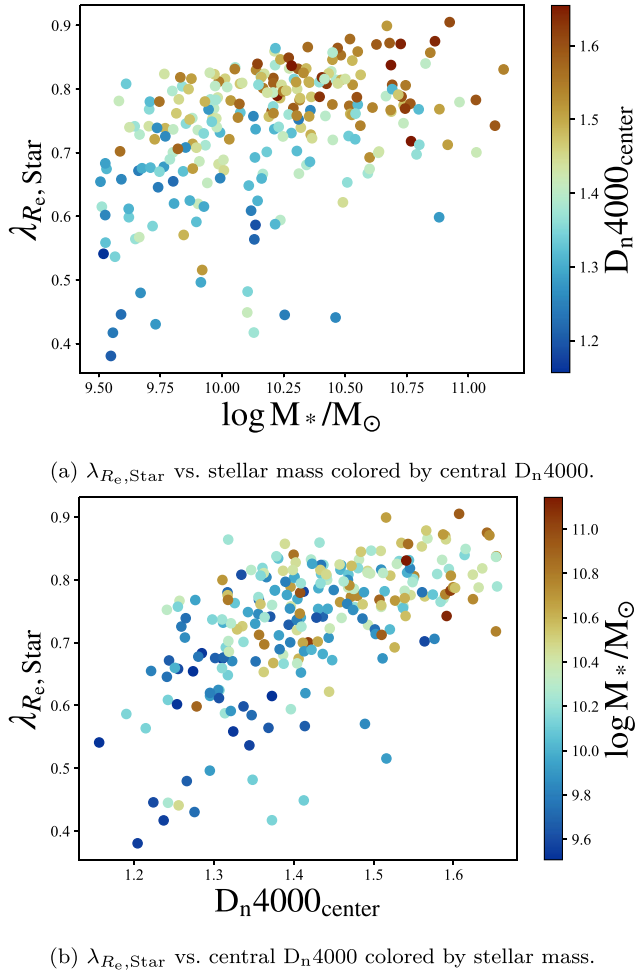


Figure 6. The correlations among $\lambda_{R_e,Star}$ stellar mass, and central D_n4000 for galaxies with $\Delta\Sigma_1 < 0$, $D_n4000_{centre} < 1.66$.

Peng & Renzini 2020; Renzini 2020). Similar processes are also visible in simulations (Lagos et al. 2017). Late-accreted gas with higher specific angular momentum can hardly reach the centre and feed the star formation there, leading to central stellar population aging with increasing mass (Renzini et al. 2018). This scenario, however, cannot explain the low-lying outliers or the strong tendency of low $\lambda_{R_e,Star}$ galaxies at a fixed mass to have low D_n4000_{centre} . Additional ideas are needed to explain these features.

As described in Section 2.3, we divide galaxies into subsets interpreted as affected by different kinds of disturbance. Galaxies flagged as having ‘perturbed kinematics’ show twist signatures in their inner velocity fields that plausibly originate from non-axisymmetric, internal mass irregularities such as bars. Galaxies denoted as having ‘disturbed morphologies’ exhibit asymmetric or clumpy structures in their images, which are more likely caused by external interactions, such as a merger or a fly-by or perhaps simply the recent arrival of a large amount of gas in one coherent blob. To further estimate the effect of external disturbances, we now also call back the star-forming merging galaxies which were rejected when choosing the sample (Section 2.3). All three samples – disturbed morphologies, perturbed kinematics, and merging galaxies – are plotted in $\lambda_{R_e,Star}$ versus D_n4000_{centre} and $\lambda_{R_e,Star}$ versus $\log M_*$ in Fig. 7. The rejected merging galaxies (limited to have $P_{MG} > 0.3$, $\log M_*/M_\odot > 9.5$) are shown as the blue stars, which are further limited to objects with

$SSFR > -10.5$ in order to ensure that all galaxies be comparably gas-rich.

Fig. 7 shows several trends. The two subsamples, perturbed kinematics and disturbed morphology, cover most of the low λ_{R_e} outliers, hence disturbance seems to be associated with low apparent rotational support. Galaxies with ‘perturbed kinematics’ (pink triangles) are more dispersed however, not only occupying low λ_{R_e} regions but also residing on the ridge line of clean sample. This suggests that internal perturbations, like bars, are less serious kinematic disturbances and do not inevitably imply low rotational support. In contrast, galaxies with ‘disturbed morphologies’ (black triangles) mainly reside in low λ_{R_e} and low D_n4000_{centre} regions, with a relatively small fraction reaching the ridgeline. Low λ_{R_e} and young D_n4000_{centre} values correlate most tightly with disturbed morphology, indicating that external disturbances usually depress $\lambda_{R_e,Star}$ and central D_n4000 . This interpretation is borne out by the distribution of clearly merging galaxies (blue stars), which lie lowest in the diagrams of all samples. Their departure from the ridgeline is in the same direction but even stronger than the disturbed galaxies. We suggest that these objects, together with the black triangles, exhibit a continuum of external interactions, with the blue stars representing the most extreme examples. These points are also illustrated by direct images in Fig. F1 which shows a montage of galaxies arranged by central D_n4000 .

We further test these inferences in by introducing S_2 , a quantitative indicator of galaxy clumpiness and asymmetry, as an indicator of external disturbance. The clumpiness parameter S_2 , defined by Simard et al. (2009), responds to all types of asymmetric structures, including bars and spiral arms, and is therefore not quite ideal for spotting mergers and major disturbances. However, the former features are more prevalent at high masses, and at the lower masses considered here, S_2 is useful. With S_2 as a disturbance indicator, the disturbance evolutionary scenario predicts decreasing S_2 with increasing central D_n4000 , and the trends should be seen at a fixed mass. In particular, the trend could be stronger for lower mass, as low-mass galaxies are more easily disturbed. Finally, this trend should be present for global D_n4000 as well as central D_n4000 , as external disturbances may enhance star formation globally as well as centrally.

Fig. 8 tests these predictions by plotting g -band S_2 versus central/global D_n4000 and also D_n4000 gradient in three mass bins, and colouring the points by $\lambda_{R_e,Star}$. The merging galaxies are also included in Fig. 8, shown as stars and coloured by $\lambda_{R_e,Star}$ as well. The results are generally consistent with these predictions. S_2_g is seen to decrease with increasing D_n4000 within each mass bin, with $\lambda_{R_e,Star}$ increasing along the trend, as expected. The trend of decreasing S_2_g is the strongest in the lowest mass bin, consistent with the scenario that low-mass galaxies are more easily disturbed. The similar trends are also visible for D_n4000 gradient in all mass bins, and D_n4000_{global} for the left mass bins, consistent with the prediction that disturbance would enhance global star formation and flatten the radial star formation gradients. The only exception is for the highest masses, where D_n4000_{global} shows almost no correlation with S_2_g , but D_n4000_{centre} and ΔD_n4000 do.

In summary, it would appear that at least two separate processes acting in concert are needed to explain all the features of low- $\Delta\Sigma_1$ galaxies as shown in Figs 6–8. A hypothetical ‘mixed scenario’ to do this is illustrated in Fig. 9, which schematically shows how low- $\Delta\Sigma_1$ galaxies might actually move in $\lambda_{R_e,Star}$ versus D_n4000_{centre} under this scenario. The red points in Fig. 9 are selected to be on the ridgeline of $\lambda_{R_e,Star}$ versus stellar mass ($\lambda_{R_e} > 0.1\log M_*/M_\odot - 0.3$). This selection reproduces the sequence in $\lambda_{R_e,Star}$ versus D_n4000 , as shown in Fig. 9. The blue points, by contrast, are low- λ_{R_e} outliers in $\lambda_{R_e,Star}$

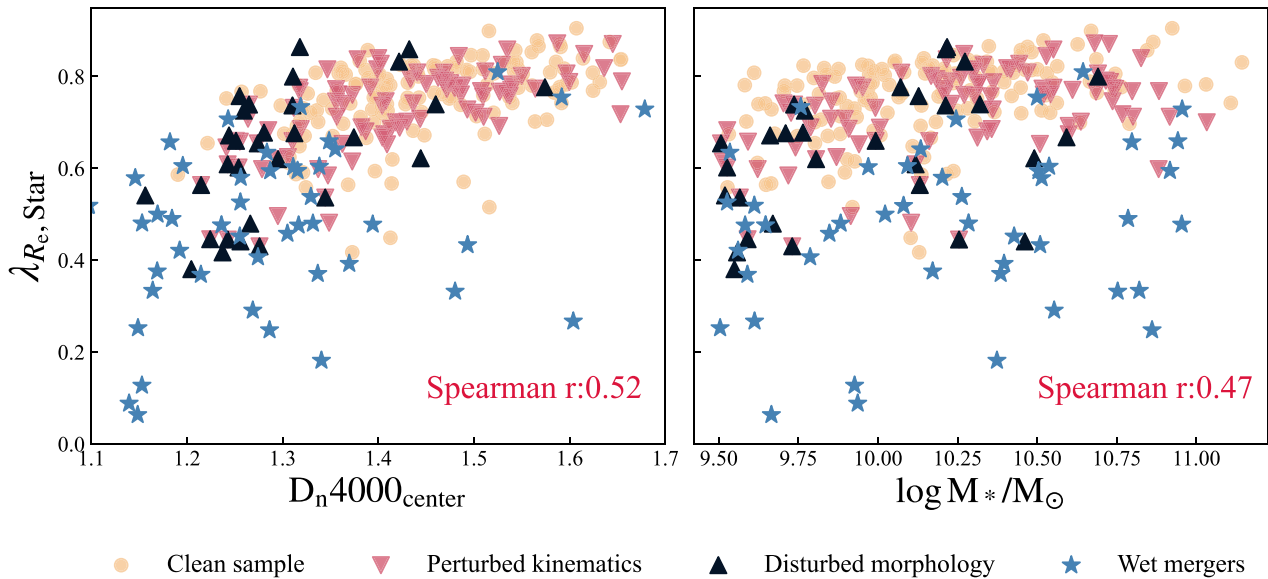


Figure 7. Replots of Fig. 6 with kinematically/morphologically disturbed galaxies tagged and star-forming merging galaxies added. Only galaxies with $\Delta\Sigma_1 < 0$ and $D_n4000_{\text{centre}} < 1.66$ are shown. Galaxies are flagged with ‘clean sample’, ‘perturbed kinematics’, and ‘disturbed morphology’ as introduced in Section 2.3. Star-forming merging galaxies are shown by the blue stars. They have $P_{\text{MG}} > 0.3$ and $\text{SSFR} > -10.5$, and are termed ‘wet mergers’ here on account of their high star formation rates. They are not part of the main sample and were excluded in plotting Fig. 6 and computing Spearman correlation coefficients. It is seen that $\lambda_{R_e, \text{Star}}$ increases more with D_n4000_{centre} than stellar mass (see Spearman correlation coefficients), and that morphologically disturbed galaxies and merging galaxies cluster at low D_n4000_{centre} . We speculate in the text that the distribution is consistent with a mixed evolutionary scenario, in which disturbances, which tend to reduce $\lambda_{R_e, \text{Star}}$ temporarily, are superimposed on an underlying evolutionary trend in which λ_{R_e} and D_n4000 increase with mass (see the text).

versus $\log M_*$. The three arrows summarize the different processes that affect galaxy $\lambda_{R_e, \text{Star}}$ and star formation state. The foundational trend is the tendency of $\lambda_{R_e, \text{Star}}$ and D_n4000_{centre} to increase as galaxies gain mass while star-forming and settle into dynamically colder, older discs, which in turn depress star formation in the centre. Superimposed on this main trend are occasional perturbations caused either by arrivals of major packets of new gas or possibly by outright mergers, dragging galaxies off the main mass-evolution ridgeline (blue arrow). These can affect galaxies of any mass but are slightly more frequent at low mass, as indicated by Fig. 7. Their tendency to generate excess central star formation makes them cluster strongly at low values of D_n4000_{centre} . Finally, the disturbed galaxies may gradually recover their kinematics and return to the high $\lambda_{R_e, \text{Star}}$ sequence by accreting more gas and forming new stars in the outer discs (purple arrow).

A potential objection to this picture is the possible impact that disturbances may have on the structure of galaxies. The model invokes such events to lower rotational support and trigger central star formation in low- $\Delta\Sigma_1$ galaxies, but at the same time such events are also credited with building central density and forming bulges (Katz 1992; Bournaud, Jog & Combes 2005). If that is severe enough, such disturbances might increase $\Delta\Sigma_1$ substantially, leaving no objects behind to populate the so-called recovery region in the low $\Delta\Sigma_1$ domain. Countering this is the fact that many low- $\Delta\Sigma_1$ galaxies are highly disturbed yet lack high-density centres, and thus mergers may not be universally efficient in making bulges. Hydro simulations also show that remnants of gas-rich mergers may be disc-dominated with bulge formation suppressed, and disc structures may be produced in later phases of mergers (Robertson et al. 2006; Hopkins et al. 2009a, b, 2010; Moster et al. 2010; Keselman & Nusser 2012; Sauvaget et al. 2018; Gargiulo et al. 2019). Therefore, low- $\Delta\Sigma_1$ galaxies may be

able to survive these processes without efficient increase in central density, contributing to the distributions seen here.

The mixed scenario contemplated in Fig. 9 may also not be a complete description of the physical processes. The key point is that at least two mechanisms seem to be required to understand the correlation of star formation rate and kinematics for low- $\Delta\Sigma_1$ galaxies, but we do not strictly rule out possibilities of other mechanisms. One possible candidate is stellar feedback. It has been seen in simulations that strong feedback can drive gas outflow, decrease central star formation and gas dispersion, and cease clump formation (El-Badry et al. 2017). Therefore, galaxies experiencing strong feedback might decrease in S_2 and increase D_n4000 and λ_{R_e} , consistent with what is shown in Fig. 8. Stellar feedback would be presented as an arrow with opposite direction to the blue arrow of disturbance in Fig. 9, and both processes may play a role in determining the distribution we see in observations. It would be interesting to further quantify the effects of different mechanisms on galaxy kinematics and star formation state.

5 DISCUSSION

5.1 Evolution on the stellar population versus central surface density plane

We turn now to the question of how galaxies evolve in the parameter space of central D_n4000 versus $\Delta\Sigma_1$.

We get clues to this from the distribution of galaxy effective radius, which is an important second factor that describes galaxy evolutionary state other than stellar mass (e.g. Mo et al. 1998; Shen et al. 2003; van der Wel et al. 2014; Cappellari 2016; Chen et al. 2020). It was first interpreted by van Dokkum et al. (2015)

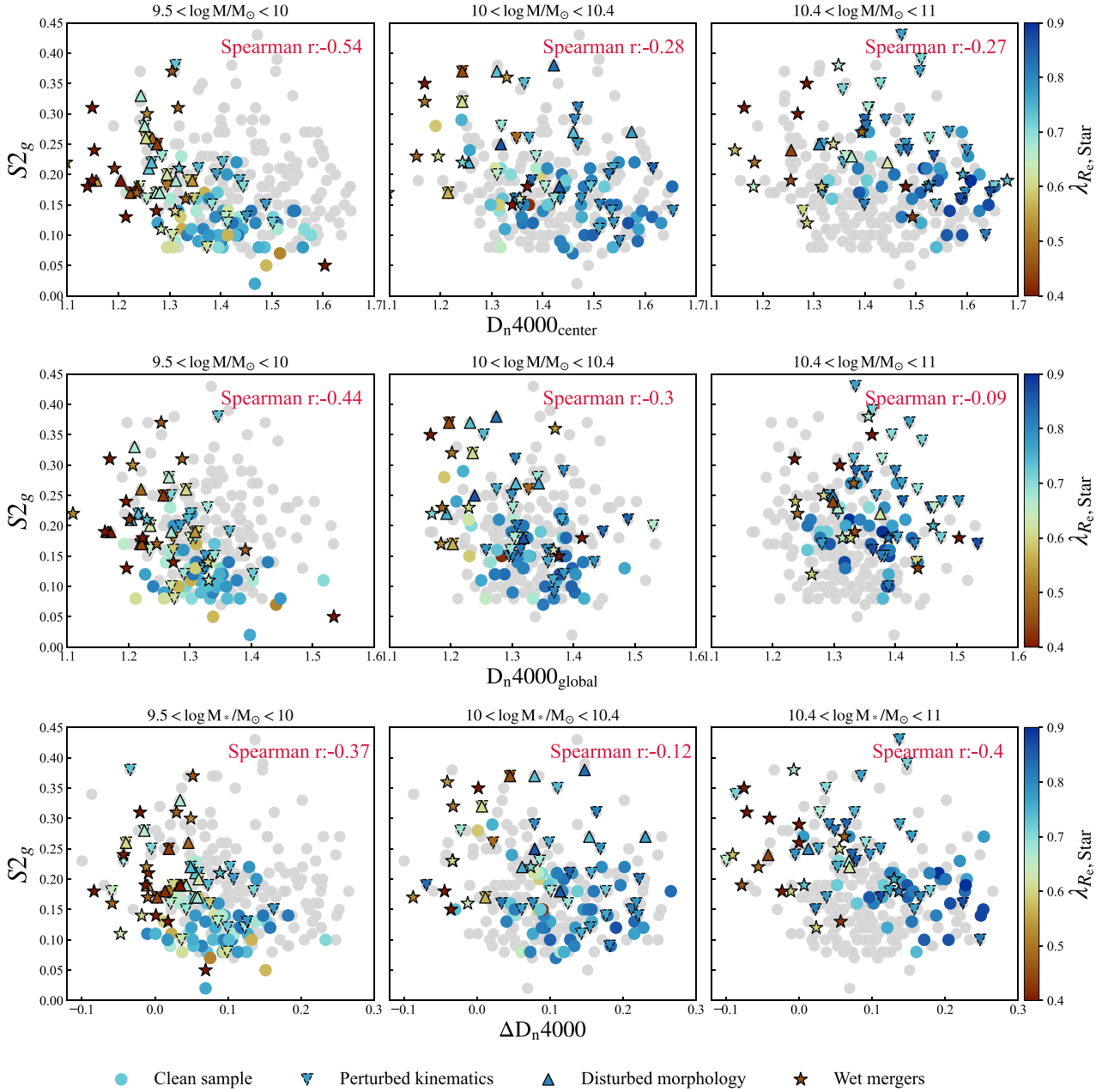


Figure 8. $S2_g$ versus D_n4000_{centre} , $D_n4000_{\text{centre}} - D_n4000_{\text{global}}$, and D_n4000_{global} , coloured by $\lambda_{R_e, \text{Star}}$ in three mass bins for star-forming low- $\Delta\Sigma_1$ galaxies ($\Delta\Sigma_1 < 0$ and $D_n4000_{\text{centre}} < 1.66$) and merging galaxies ($P_{\text{MG}} > 0.3$, $\text{SSFR} > -10.5$). The grey points on the background are the whole sample of galaxies with $\Delta\Sigma_1 < 0$ and $D_n4000_{\text{centre}} < 1.66$. The merging galaxies are shown as stars, and are excluded when computing Spearman correlation coefficients. From left to right, the coloured points are $9.5 < \log M_*/M_\odot < 10$, $9.5 < \log M_*/M_\odot < 10.4$, and $10.4 < \log M_*/M_\odot < 11$. In each mass bin, $S2_g$ decreases both with D_n4000_{centre} and ΔD_n4000 , with $\lambda_{R_e, \text{Star}}$ increasing. Similar trends are also seen in low and middle mass bins for D_n4000_{global} . The behaviour of $S2_g$, $\lambda_{R_e, \text{Star}}$, and D_n4000 in each mass bin is consistent with the scenario that galaxies are disturbed and undergo central star formation.

that galaxies may evolve along parallel tracks along $\log R_e - \log M_*$ when star forming before they meet the boundary of quenching. The picture was further developed with observations (e.g. Lilly & Carollo 2016; Chen et al. 2020), and similar evolutionary tracks that galaxies averagely increase R_e with parallel slopes on $\log R_e - \log M_*$ are also seen in simulations (Genel et al. 2018) and empirical models (Rodríguez-Puebla et al. 2017).

As the whole distribution of galaxies on $R_e - M_*$ is also moving to the upper regions with time (van der Wel et al. 2014), a reasonable

assumption that combines these properties is that galaxies may maintain their relative position in the distribution of radii at fixed mass as they evolve. In other words, galaxies with similar ranks of radii but different masses would be evolutionarily related, and the properties of the massive ones may predict the future of the less massive ones on that rank.

To see how galaxies evolve in central $D_n4000 - \Delta\Sigma_1$ under this assumption, we colour the points with LOESS smoothed half-mass radii on $D_n4000 - \Delta\Sigma_1$ in the bottom panel of Fig. 10. The points in the

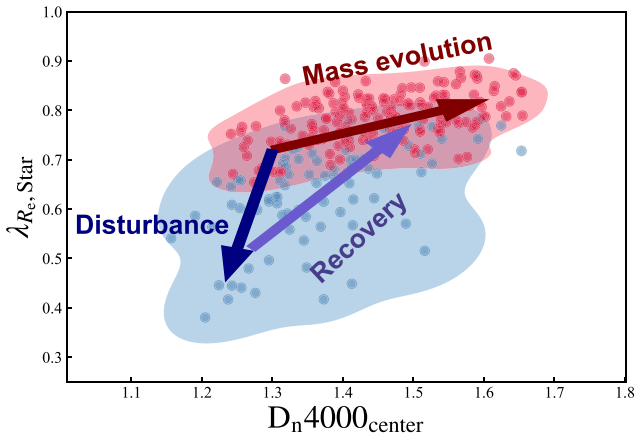


Figure 9. Schematic summary of possible evolutionary paths under a mixed-scenario model for galaxies with negative $\Delta\Sigma_1$ and $D_n4000_{\text{centre}} < 1.66$ in $\lambda_{R_e, \text{Star}}$ versus D_n4000_{centre} diagram. The red points are defined as top sequence in the $\lambda_{R_e, \text{Star}}$ versus M_* plot. The red arrow shows the evolution revealed by stellar mass, whereby rotational support and central age increase. The dark blue arrow illustrates how disturbances might effectively drag a galaxy to low $\lambda_{R_e, \text{Star}}$ and D_n4000_{centre} values. The disturbed galaxies can gradually recover spin by forming new stars from late-accreting, high-angular momentum gas, thereby getting back to the sequence along the light purple arrow.

top panel as complement are coloured by LOESS smoothed $\lambda_{R_e, \text{Star}}$ values, same as in the lower right panel of Fig. 4. Schematic evolutionary tracks under the assumption of constant radius rankings are represented as the slanted arrows (solid black arrows), along which R_{50} keeps approximately constant. Therefore, if the assumption is true, galaxies would evolve on almost parallel tracks in $D_n4000_{\text{centre}} - \Delta\Sigma_1$ before they quench, with a strong inclined slope along which both D_n4000_{centre} and $\Delta\Sigma_1$ increase. In contrast, $\lambda_{R_e, \text{Star}}$ evolves non-monotonically, increasing while galaxies are star-forming and then declining when they quench. The early, increasing phases are consistent with the rise in λ_{R_e} with mass (for low- $\Delta\Sigma_1$ galaxies) in Figs 6 and 7, and the general picture of rise and then fall versus mass has been shown in many works (e.g. Falcón-Barroso et al. 2019; Wang et al. 2020; Fraser-McKelvie et al. 2021).

This evolutionary scenario differs from that proposed by Luo et al. (2020), who argued that galaxies evolve through the elbow shape en route to quenching. Their path is shown as the translucent grey arrows in Fig. 10, along which galaxies increase $\Delta\Sigma_1$ first with D_n4000 almost constant, and then decline in star formation rates with $\Delta\Sigma_1$ almost unchanged. Luo et al. (2020) proposed that the first (horizontal) process might result from secular evolution (Kormendy & Kennicutt 2004; Fang et al. 2013), whereby non-circular mass distributions like bars would torque the gas, causing it to flow to the centre, make stars and build Σ_1 (Wang et al. 2012; Lin et al. 2017; Querejeta et al. 2021). However, the new finding in Fig. 10 is that half-mass radii also strongly decrease along that arrow, by almost a full dex (see also Fig. 3), and it is not clear whether secular evolution alone could cause such a change. If secular processes are limited to stars alone, then energy and angular momentum are conserved and some stars move outward as other stars move inward (Lynden-Bell & Kalnajs 1972; Kormendy & Kennicutt 2004), thus causing little net change in half-mass radius. If gas is brought in along with stars, the ensuing star formation at the centre may cause the half-mass radius to shrink. However, the overall light distributions of these objects are highly compact; they lack the extended envelope of light that would

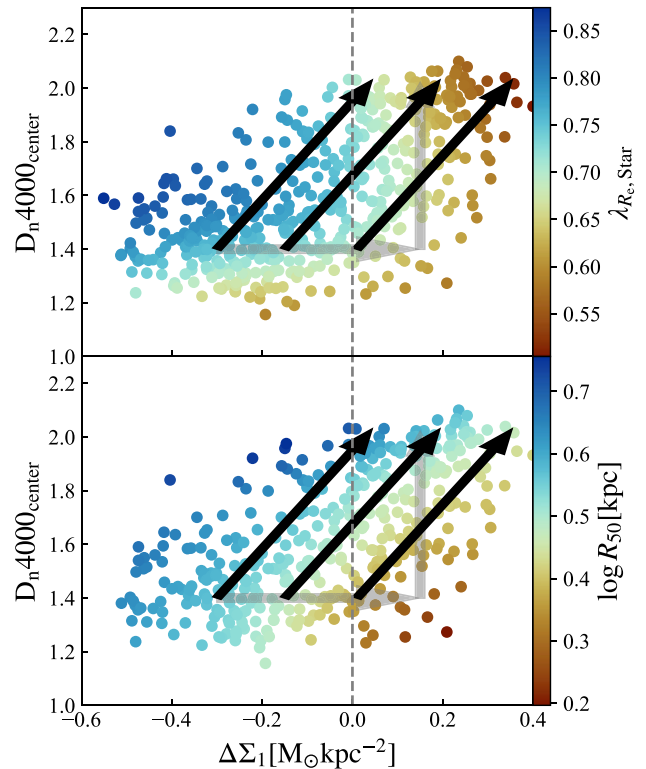


Figure 10. Schematic summary of evolutionary paths on the D_n4000_{centre} versus $\Delta\Sigma_1$ space. The top panel is coloured by LOESS smoothed $\lambda_{R_e, \text{Star}}$ and the bottom panel is coloured by smoothed half-mass radii. The grey horizontal and vertical arrows show the hypothesized paths that galaxies first increase relative central densities with stellar population ages almost constant, and then quench with $\Delta\Sigma_1$ almost unchanged. This scenario is challenged by the effectively reduced R_{50} along the horizontal path, and the black slanted arrows represent an alternative scenario that galaxies maintain their relative ranks of half-mass radii. Under this scenario, the wholesale evolution of pseudo-bulge galaxies into classical-bulge galaxies is not preferred (see the text).

be produced by conservation of angular momentum during secular evolution.

An alternative process to increase central density is wet mergers, which may be able to cause gas inflow and strong shrinkage in size. This process, called ‘compaction’, is common in simulations of gas-rich galaxies (Dekel & Burkert 2014; Ceverino et al. 2015; Zolotov et al. 2015; Tacchella et al. 2016; Barro et al. 2017) and has been invoked to account for the small radii of quenched galaxies at $z \sim 2$ (Barro et al. 2017). However, this process is less likely to explain elbow galaxies today. First, gas contents are much lower now than they were at $z \sim 2$, and second, the elbow galaxies are common being the smallest star-forming galaxies at every mass. Compaction may have played a role in their formation in the distant past, but the Luo et al. (2020) arrow in Fig. 10 is meant to indicate today. The notion that large-radii galaxies are evolving en masse to make small galaxies today is inconsistent with numerous data, such as the spread in star-forming galaxy radii at fixed mass, which has been remarkably constant since $z \sim 2$ (van der Wel et al. 2014).

We do acknowledge that the black arrows in Fig. 10 are not to be taken literally as accurate evolutionary paths, not only due to the limited sample size but also to the drifting of whole data in all diagrams over time. Even so, the arrows may still be a guide to how

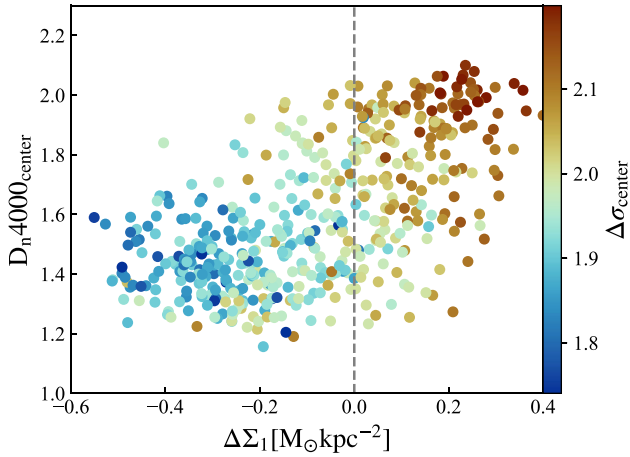


Figure 11. Distribution of a kinematic bulge-indicator, $\Delta\sigma_{\text{centre}} \equiv \log \sigma_{\text{centre}} - 0.25(\log M_* - 10.5)$, in D_n4000_{centre} versus $\Delta\Sigma_1$. The distribution of $\Delta\sigma_{\text{centre}}$ is consistent with the J-shape pattern shown by $\lambda_{R_c, \text{Star}}$. Most of the red points are to the right of the $\Delta\Sigma_1$ boundary, with blue points to the left, indicating that $\Delta\Sigma_1$ does a fairly good job of separating bulges characterized by kinematics. The exception is for the points on the bottom with relatively high $\Delta\sigma_{\text{centre}}$, located to the left of $\Delta\Sigma_1 = 0$. Nevertheless, if the evolutionary tracks in Fig. 11 are correct, $\Delta\Sigma_1$ turns out to be useful in separating bulge types and the wholesale evolution of pseudo-bulge galaxies into classical-bulge galaxies is not preferred (see the text).

objects will evolve in relation to one another, and thus to the picture of relative paths in D_n4000 – $\Delta\Sigma_1$ space. It will be interesting to see whether future simulations can reproduce the joint distributions of kinematic properties, star formation rates, and radii seen today and back in time, and in particular to test the assumption that galaxies with similar radius rankings are evolutionarily linked.

5.2 The evolutionary relationship of pseudo-bulges and classical bulges

We close this discussion on evolution with a brief mention of the possible implications of our findings for the evolution of bulges. This was a major topic in Luo et al. (2020), which asserted that $\Delta\Sigma_1 = 0$ could be used as the dividing line between pseudo-bulges and classical-bulges and proceeded to argue, as we said above, that pseudo-bulges en masse evolve into the elbow region to become classical bulges. If we take that definition of bulge types, the assumption of constant radii rankings, however, holds an opposite view that most pseudo-bulges will not evolve to classical bulges in general before they quench.

To this point, we have not mentioned the word ‘bulge’ since measurements of bulge type and bulge prominence are rather technical (e.g. Kormendy & Kennicutt 2004; Fisher & Drory 2008; Gadotti 2009; Kormendy 2016). Moreover, it is probable that the use of $\Delta\Sigma_1 = 0$ as the dividing line is not exact; Luo et al. (2020) compared $\Delta\Sigma_1$ with more precise bulge measurements by Gadotti (2009), and while the agreement was good, it was not perfect. But MaNGA data add dynamical estimates of bulge prominence to the space of D_n4000 versus $\Delta\Sigma_1$, permitting us to take a new look at the accuracy of $\Delta\Sigma_1$ in classifying bulges and at the same time reconsider whether pseudo-bulges evolve to classical bulges.

Fig. 11 plots a simple dynamical parameter, $\log \sigma_{\text{centre}} - 0.25 \log M_*$ in D_n4000 versus $\Delta\Sigma_1$ to indicate bulge types, as central dispersion should be sensitive to bulge prominence (Kormendy &

Kennicutt 2004; Fabricius et al. 2012; Zhao 2012; Fisher & Drory 2016; Sachdeva et al. 2020; Hu et al. 2024). This parameter removes the general trend of all velocities to increase roughly as $M_*^{0.25}$. As shown in Fig. 11, classical bulge candidates (high $\Delta\Sigma_1$) have relative high central dispersions, while pseudo-bulge candidates (low $\Delta\Sigma_1$) have relatively low central dispersions.

This new colour pattern strongly resembles the J-shaped pattern in Fig. 4, which is not unexpected since λ_{R_c} and velocity dispersion should correlate inversely. Furthermore, the dividing line $\Delta\Sigma_1 = 0$ actually does a reasonable job to first order of separating bulge candidates indicated by kinematics: classical-bulges (red) lie generally to the right and pseudo-bulges (blue) lie generally to the left. The boundary of $\Delta\Sigma_1 = 0$ corresponds to $\Delta\sigma_{\text{centre}} \sim 2$, consistent with the classifications in Sachdeva et al. (2020) and Hu et al. (2024). In more detail, however, a population of relatively high- $\Delta\sigma$ galaxies is seen to run along the lower edge of the distribution on the left-hand side. These points are on the ‘wrong’ side of $\Delta\Sigma_1$. They lie near the bottom of the middle arrow in Fig. 10 and consist of low-mass star-forming galaxies with intermediate radii and borderline high relative central σ . If the arrows in Fig. 10 are correct, their bulge prominence (characterized by kinematics) will actually decline in future as they gain new mass in the form of dynamically cold discs (i.e. they are low-mass galaxies on the ridgeline in Fig. 6). These objects do not fit the profile of ‘classical bulges’ as commonly understood, and if they are ignored, then $\Delta\Sigma_1 = 0$ turns out to be a useful dividing line between the two types of bulges. Regardless, however, the main point still stands: if the tilted arrows in Fig. 10 are correct, some borderline pseudo-bulges may become classical bulges, but the wholesale evolution of all pseudo-bulges to classical bulges does not appear to be correct.

5.3 Caveats

5.3.1 Lack of spectral resolution for low dispersion

Learning kinematics of disc galaxies is limited by spectral resolution. The instrumental dispersion of MaNGA survey is $\sim 67 \text{ km s}^{-1}$, and the stellar dispersion measurement is suggested to be reliable down to 50 km s^{-1} when $S/N > 10$ (Westfall et al. 2019). However, many studies have found that dispersion may be overestimated when lower than instrumental dispersion (e.g. Falc3n-Barroso et al. 2017). Dispersion measurement is biased and the measured λ_{R_c} is a ‘lower limit’ of the true values. This could introduce artificial effects on the relations we see.

A check on our results is whether they are similar in both gas and stellar kinematics. The instrumental effect is less severe for gas measurements, since the S/N of emission line can be much higher than that of continuum for star forming galaxies. A comparison between MaNGA and DiskMass survey ($R \sim 10000$, Bershady et al. 2010) shows that for MPL10 and later versions the observed $H\alpha$ dispersion is not significantly biased in the region of $4 \text{ arcsec} < r < 15 \text{ arcsec}$, where typical $H\alpha$ dispersion are $\sim 20 \text{ km s}^{-1}$ and are much lower than the instrumental dispersion (Law et al. 2021). Therefore, if the results of stellar kinematics are reproduced in gas kinematics, they are likely to be real.

We checked the results for gas kinematics and show the figures in Appendix D. The patterns of λ_{R_c} on D_n4000 – $\Delta\Sigma_1$ plot are both seen for stellar and gas kinematics and we propose they are likely to be correct. Though the relation between mass and λ_{R_c} for low- $\Delta\Sigma_1$ galaxies is not clear for gas (Fig. D2a), it could be true given that gas is dissipational and more settled. In previous studies of SAMI and CALIFA, similar dependence of stellar λ_{R_c} on mass was seen

(Falc3n-Barroso et al. 2019; Fraser-McKelvie et al. 2021; van de Sande et al. 2021a, b; Cortese et al. 2022), and we believe it is real. In conclusion, all of our important conclusions ARE reproduced in stars and gas if appropriate allowance is made for the greater dissipational behaviour of gas. While these results should be further validated through future tests with higher resolution, we have confidence in their overall validity.

5.3.2 Lack of spatial resolution for small galaxies

Another important effect in kinematic measurements is from the limited spatial resolution. Low spatial resolution can flatten velocity and dispersion profiles, resulting in underestimation of λ_{R_e} . We limit the sample to have $R_e > 5$ arcsec and do not apply any correction. In Appendix B, we show that under our sample selection, the effect of low spatial resolution is not severe and could be neglected without correction.

5.3.3 Selection bias for high- $\Delta\Sigma_1$ galaxies

Although the restriction of the sample to objects with $R_e > 5$ arcsec mitigates the spatial resolution problem, the selection itself can make the sample biased. The excluded small galaxies ($R_e < 5$ arcsec) only make up a relatively small fraction (~ 25 per cent) of low- $\Delta\Sigma_1$ galaxies, but a considerable fraction (~ 67 per cent) of high- $\Delta\Sigma_1$ galaxies. The selection bias does not largely affect our conclusions of low- $\Delta\Sigma_1$ galaxies, but makes it hard to interpret evolution for high- $\Delta\Sigma_1$ galaxies. Moreover, as indicated in Fig. 3, high- $\Delta\Sigma_1$ galaxies is a composite category with a large range of star formation rates. We do not give detailed interpretations of high- $\Delta\Sigma_1$ galaxies in this paper, and plan to address these issues in a future work (Wang et al. in preparation).

6 CONCLUSIONS

In this paper, we show how galaxy rotational support varies as a function of stellar population age and central surface densities with ~ 500 galaxies from MaNGA. With $\Delta\Sigma_1$ and D_n4000 as structural and stellar population indicators, we show that the rotational support correlates with central and global properties in a complex manner. The main results are as follows:

(i) We confirm the conclusions of many previous works that rotational support ($\lambda_{R_e, \text{Star}}$) statistically decreases with relative central density ($\Delta\Sigma_1$) and stellar population age (D_n4000) with some mass dependence as well (Figs 4 and 5). For the first order, $\Delta\Sigma_1$ and D_n4000 increase with stellar mass with $\lambda_{R_e, \text{Star}}$ decreasing.

(ii) The above trends exist in a large smooth landscape, in which rotational support increases with central/global stellar population age when $\Delta\Sigma_1$ is low and decreases with $\Delta\Sigma_1$ and global stellar population when $\Delta\Sigma_1$ is high (Fig. 4). This landscape is visible as a smooth ‘J-shape’ pattern on the 2D landscape of central properties, D_n4000_{centre} versus $\Delta\Sigma_1$, and as smooth tilted stripes (a fainter ‘J-shape’) on the landscape of global D_n4000 versus $\Delta\Sigma_1$. Specifically, in low- $\Delta\Sigma_1$ galaxies, λ_{R_e} increases with both central and global D_n4000 , but shows a stronger correlation with central stellar population properties (Figs 4 and 5). For high- $\Delta\Sigma_1$ galaxies, λ_{R_e} decreases more with global D_n4000 but shows a weak dependence on central D_n4000 (Figs 4 and 5). These specific features are largely independent of stellar mass. The new patterns indicate that a combination of stellar populations and structures is needed to characterize the rotational support more completely.

(iii) For low- $\Delta\Sigma_1$ galaxies, plots of $\lambda_{R_e, \text{Star}}$ versus mass and central D_n4000 show a ridgeline of morphologically normal galaxies plus points scattered to lower λ_{R_e} by disturbances (Figs 4–7). Along the ridgeline λ_{R_e} increases with central stellar population ages and stellar mass. The low- $\lambda_{R_e, \text{Star}}$ outliers are either morphologically or kinematically disturbed, and the interacting galaxies with strong mergers in process show markedly lower $\lambda_{R_e, \text{Star}}$ (Figs 7 and 8). Moreover, galaxies with disturbed morphologies or strong mergers also tend to have low central D_n4000 (Figs 7 and 8, and Fig. F1).

(iv) For low- $\Delta\Sigma_1$ galaxies, the properties described in (iv) and their relationships are consistent with a ‘mixed’ evolutionary model (Fig. 9). In this model, disturbance effects are superimposed on an underlying evolutionary trend where $\lambda_{R_e, \text{Star}}$ and D_n4000_{centre} increase with mass. The increasing trend of rotational support with mass, where galaxies get kinematically and morphologically settled, is consistent with a picture in which galaxies become more and more settled as they grow in mass. At a fixed mass, galaxies with low λ_{R_e} may have experienced mergers or instabilities, which introduce disturbance, feed central star formation with accreted gas and flatten D_n4000 profiles.

(v) Low- $\Delta\Sigma_1$ galaxies have systematically larger half-mass radii than high- $\Delta\Sigma_1$ galaxies at a fixed mass (Fig. 3). Under the assumption that galaxies have maintained their relative rankings in radius in recent times, we plot schematic evolutionary paths for star-forming galaxies in the space of D_n4000_{centre} versus $\Delta\Sigma_1$ (Fig. 10). Galaxies with different radii follow steep paths in which D_n4000_{centre} increases greatly as they age whereas $\Delta\Sigma_1$ increases only modestly. Applying this conclusion to different bulge types, we infer that pseudo-bulges and classical bulges are on different evolutionary paths and remain separate at least until quenching (Figs 10 and 11).

The results in this paper add more information substantially to this existing body of data, which already show the complex behaviours and interplay of structural, stellar population and kinematic properties. In the future, simulations and observations with high resolution can be useful for understanding dynamical processes and star formation histories in galaxy evolution. Upcoming IFS surveys in the future can also provide more detailed information about galaxy spatial population and kinematics. It would be important to investigate the physical processes that produce the observed distributions, and to test the assumption where galaxies maintain their relative ranks of radii in future simulations.

ACKNOWLEDGEMENTS

This work is partly supported by the National Key Research and Development Program of China (no. 2018YFA0404501 to SM), by the National Natural Science Foundation of China (grant no. and 11821303 to SM). We would like to thank Drs Dandan Xu and Song Huang and an anonymous referee for constructive and insightful suggestions and comments which greatly improved the paper. We express appreciation for the scientific colour maps provided by cmcrameri and cmasher, and acknowledge the use of the TOPCAT³ plotting and data analysis tool, which proved indispensable.

Funding for the Sloan Digital Sky Survey IV has been provided by the Alfred P. Sloan Foundation, the U.S. Department of Energy Office of Science, and the Participating Institutions. SDSS-IV acknowledges support and resources from the Center for High Performance Computing at the University of Utah. The SDSS

³<http://www.starlink.ac.uk/topcat/>

website is www.sdss4.org. SDSS-IV is managed by the Astrophysical Research Consortium for the Participating Institutions of the SDSS Collaboration including the Brazilian Participation Group, the Carnegie Institution for Science, Carnegie Mellon University, Center for Astrophysics Harvard and Smithsonian, the Chilean Participation Group, the French Participation Group, Instituto de Astrofísica de Canarias, The Johns Hopkins University, Kavli Institute for the Physics and Mathematics of the Universe (IPMU)/University of Tokyo, the Korean Participation Group, Lawrence Berkeley National Laboratory, Leibniz Institut für Astrophysik Potsdam (AIP), Max-Planck-Institut für Astronomie (MPIA Heidelberg), Max-Planck-Institut für Astrophysik (MPA Garching), Max-Planck-Institut für Extraterrestrische Physik (MPE), National Astronomical Observatories of China, New Mexico State University, New York University, University of Notre Dame, Observatório Nacional/MCTI, The Ohio State University, Pennsylvania State University, Shanghai Astronomical Observatory, United Kingdom Participation Group, Universidad Nacional Autónoma de México, University of Arizona, University of Colorado Boulder, University of Oxford, University of Portsmouth, University of Utah, University of Virginia, University of Washington, University of Wisconsin, Vanderbilt University, and Yale University.

JGF-T gratefully acknowledges the grant support provided by Proyecto Fondecyt Iniciación no. 11220340, and from the Joint Committee ESO-Government of Chile 2021 (ORP 023/2021), and from Becas Santander Movilidad Internacional Profesores 2022, Banco Santander Chile.

NFB acknowledges Science and Technologies Facilities Council (STFC) grant ST/V000861/1.

DATA AVAILABILITY

The data presented in this paper are available upon request for legitimate scientific purposes.

REFERENCES

- Abazajian K. N. et al., 2009, *ApJS*, 182, 543
 Abdurro'uf et al., 2022, *ApJS*, 259, 35
 Bacon R. et al., 2001, *MNRAS*, 326, 23
 Barro G. et al., 2017, *ApJ*, 840, 47
 Baugh C. M., 2006, *Rep. Prog. Phys.*, 69, 3101
 Belfiore F. et al., 2019, *AJ*, 158, 160
 Bershad Y. A., Verheijen M. A. W., Swaters R. A., Andersen D. R., Westfall K. B., Martinsson T., 2010, *ApJ*, 716, 198
 Blanton M. R., Kazin E., Muna D., Weaver B. A., Price-Whelan A., 2011, *AJ*, 142, 31
 Bluck A. F. L., Mendel J. T., Ellison S. L., Moreno J., Simard L., Patton D. R., Starkeburg E., 2014, *MNRAS*, 441, 599
 Bournaud F., Jog C. J., Combes F., 2005, *A&A*, 437, 69
 Brough S. et al., 2017, *ApJ*, 844, 59
 Bundy K. et al., 2014, *ApJ*, 798, 7
 Cappellari M., 2016, *ARA&A*, 54, 597
 Cappellari M., 2017, *MNRAS*, 466, 798
 Cappellari M., Emsellem E., 2004, *PASP*, 116, 138
 Cappellari M. et al., 2011, *MNRAS*, 413, 813
 Cappellari M. et al., 2013, *MNRAS*, 432, 1862
 Ceverino D., Dekel A., Tweed D., Primack J., 2015, *MNRAS*, 447, 3291
 Chen Z. et al., 2020, *ApJ*, 897, 102
 Cheung E. et al., 2012, *ApJ*, 760, 131
 Cleveland W. S., Devlin S. J., 1988, *J. Am. Stat. Assoc.*, 83, 596
 Cole S., Aragon-Salamanca A., Frenk C. S., Navarro J. F., Zepf S. E., 1994, *MNRAS*, 271, 781
 Cortese L. et al., 2016, *MNRAS*, 463, 170
 Cortese L. et al., 2022, *MNRAS*, 513, 3709
 Croom S. M. et al., 2012, *MNRAS*, 421, 872
 Croom S. M. et al., 2021, *MNRAS*, 505, 2247
 de Zeeuw P. T. et al., 2002, *MNRAS*, 329, 513
 Dekel A., Burkert A., 2014, *MNRAS*, 438, 1870
 Drory N. et al., 2015, *AJ*, 149, 77
 El-Badry K., Wetzel A. R., Geha M., Quataert E., Hopkins P. F., Kereš D., Chan T. K., Faucher-Giguère C.-A., 2017, *ApJ*, 835, 193
 Emsellem E. et al., 2007, *MNRAS*, 379, 401
 Fabricius M. H., Saglia R. P., Fisher D. B., Drory N., Bender R., Hopp U., 2012, *ApJ*, 754, 67
 Falcón-Barroso J. et al., 2017, *A&A*, 597, A48
 Falcón-Barroso J. et al., 2019, *A&A*, 632, A59
 Fang J. J., Faber S. M., Koo D. C., Dekel A., 2013, *ApJ*, 776, 63
 Fisher D. B., 2006, *ApJ*, 642, L17
 Fisher D. B., Drory N., 2008, *AJ*, 136, 773
 Fisher D. B., Drory N., 2010, *ApJ*, 716, 942
 Fisher D. B., Drory N., 2016, in Laurikainen E., Peletier R., Gadotti D., eds, *Galactic Bulges, Astrophysics and Space Science Library (ASSL)*, Vol. 41. Springer International Publishing, Cham, p. 41
 Fraser-McKelvie A. et al., 2021, *MNRAS*, 503, 4992
 Fraser-McKelvie A., Cortese L., 2022, *ApJ*, 937, 117
 Gadotti D. A., 2009, *MNRAS*, 393, 1531
 Gargiulo I. D. et al., 2019, *MNRAS*, 489, 5742
 Genel S. et al., 2018, *MNRAS*, 474, 3976
 Goddard D. et al., 2017, *MNRAS*, 466, 4731
 González Delgado R. M. et al., 2015, *A&A*, 581, A103
 Graham M. T. et al., 2018, *MNRAS*, 477, 4711
 Greene J. E. et al., 2018, *ApJ*, 852, 36
 Gunn J. E. et al., 2006, *AJ*, 131, 2332
 Harborne K. E., van de Sande J., Cortese L., Power C., Robotham A. S. G., Lagos C. D. P., Croom S., 2020, *MNRAS*, 497, 2018
 Hernquist L., 1992, *ApJ*, 400, 460
 Holmberg E., 1958, *Meddelanden fran Lunds Astronomiska Observatorium Serie II*, 136, 1
 Hopkins P. F. et al., 2009a, *MNRAS*, 397, 802
 Hopkins P. F., Cox T. J., Younger J. D., Hernquist L., 2009b, *ApJ*, 691, 1168
 Hopkins P. F. et al., 2010, *ApJ*, 715, 202
 Hopkins P. F., Cox T. J., Hernquist L., Narayanan D., Hayward C. C., Murray N., 2013, *MNRAS*, 430, 1901
 Hu J., Wang L., Ge J., Zhu K., Zeng G., 2024, *MNRAS*, 529, 4565
 Kassin S. A. et al., 2012, *ApJ*, 758, 106
 Katz N., 1992, *ApJ*, 391, 502
 Kauffmann G. et al., 2003a, *MNRAS*, 341, 33
 Kauffmann G. et al., 2003b, *MNRAS*, 341, 54
 Keselman J. A., Nusser A., 2012, *MNRAS*, 424, 1232
 Kormendy J., 2016, in Laurikainen E., Peletier R., Gadotti D., eds, *Galactic Bulges, Astrophysics and Space Science Library*, Vol. 418. Springer, Cham, p. 431
 Kormendy J., Kennicutt Robert C. J., 2004, *ARA&A*, 42, 603
 Kormendy J., Fisher D. B., Cornell M. E., Bender R., 2009, *ApJS*, 182, 216
 Krajnović D. et al., 2011, *MNRAS*, 414, 2923
 Lagos C. d. P., Theuns T., Stevens A. R. H., Cortese L., Padilla N. D., Davis T. A., Contreras S., Croton D., 2017, *MNRAS*, 464, 3850
 Law D. R. et al., 2021, *AJ*, 161, 52
 Lee B. et al., 2018, *ApJ*, 853, 131
 Lee Y. S. et al., 2011, *ApJ*, 738, 187
 Lilly S. J., Carollo C. M., 2016, *ApJ*, 833, 1
 Lin L., Li C., He Y., Xiao T., Wang E., 2017, *ApJ*, 838, 105
 Lintott C. et al., 2011, *MNRAS*, 410, 166
 Luo Y. et al., 2020, *MNRAS*, 493, 1686
 Lynden-Bell D., Kalnajs A. J., 1972, *MNRAS*, 157, 1
 Martig M., Bournaud F., Teyssier R., Dekel A., 2009, *ApJ*, 707, 250
 Mo H. J., Mao S., White S. D. M., 1998, *MNRAS*, 295, 319
 Morselli L., Popesso P., Erfanianfar G., Concas A., 2017, *A&A*, 597, A97
 Mosser B. P., Macciò A. V., Somerville R. S., Johansson P. H., Naab T., 2010, *MNRAS*, 403, 1009
 Naab T., Khochfar S., Burkert A., 2006, *ApJ*, 636, L81
 Naab T., Johansson P. H., Ostriker J. P., 2009, *ApJ*, 699, L178

- Neumann J. et al., 2022, *MNRAS*, 513, 5988
 Oh S. et al., 2020, *MNRAS*, 495, 4638
 Padilla N. D., Strauss M. A., 2008, *MNRAS*, 388, 1321
 Peng Y.-j. et al., 2010, *ApJ*, 721, 193
 Peng Y.-j., Renzini A., 2020, *MNRAS*, 491, L51
 Querejeta M. et al., 2015, *A&A*, 579, L2
 Querejeta M. et al., 2021, *A&A*, 656, A133
 Renzini A., 2020, *MNRAS*, 495, L42
 Renzini A. et al., 2018, *ApJ*, 863, 16
 Robertson B., Bullock J. S., Cox T. J., Di Matteo T., Hernquist L., Springel V., Yoshida N., 2006, *ApJ*, 645, 986
 Rodríguez S., Padilla N. D., 2013, *MNRAS*, 434, 2153
 Rodríguez-Puebla A., Primack J. R., Avila-Reese V., Faber S. M., 2017, *MNRAS*, 470, 651
 Sachdeva S., Ho L. C., Li Y. A., Shankar F., 2020, *ApJ*, 899, 89
 Sánchez S. F. et al., 2012, *A&A*, 538, A8
 Sauvagat T., Hammer F., Puech M., Yang Y. B., Flores H., Rodrigues M., 2018, *MNRAS*, 473, 2521
 Schade D., Lilly S. J., Crampton D., Hammer F., Le Fevre O., Tresse L., 1995, *ApJ*, 451, L1
 Sharma S. et al., 2014, *ApJ*, 793, 51
 Shen S., Mo H. J., White S. D. M., Blanton M. R., Kauffmann G., Voges W., Brinkmann J., Csabai I., 2003, *MNRAS*, 343, 978
 Simard L. et al., 2002, *ApJS*, 142, 1
 Simard L. et al., 2009, *A&A*, 508, 1141
 Simard L., Mendel J. T., Patton D. R., Ellison S. L., McConnell A. W., 2011, *ApJS*, 196, 11
 Simons R. C. et al., 2017, *ApJ*, 843, 46
 Smee S. A. et al., 2013, *AJ*, 146, 32
 Springel V., Di Matteo T., Hernquist L., 2005, *ApJ*, 620, L79
 Tacchella S., Dekel A., Carollo C. M., Ceverino D., DeGraf C., Lapiner S., Mandelker N., Primack J. R., 2016, *MNRAS*, 458, 242
 Toomre A., 1977, in Tinsley B. M., Larson Richard B., Gehret D. C., eds, *Evolution of Galaxies and Stellar Populations*. Yale University Observatory, New Haven, p. 401
 Unterborn C. T., Ryden B. S., 2008, *ApJ*, 687, 976
 van de Sande J. et al., 2017, *MNRAS*, 472, 1272
 van de Sande J. et al., 2018, *Nat. Astron.*, 2, 483
 van de Sande J. et al., 2021a, *MNRAS*, 505, 3078
 van de Sande J. et al., 2021b, *MNRAS*, 508, 2307
 van der Wel A. et al., 2014, *ApJ*, 788, 28
 van Dokkum P. G. et al., 2015, *ApJ*, 813, 23
 Veale M., Ma C.-P., Greene J. E., Thomas J., Blakeslee J. P., McConnell N., Walsh J. L., Ito J., 2017, *MNRAS*, 471, 1428
 Wake D. A. et al., 2017, *AJ*, 154, 86
 Wang B., Cappellari M., Peng Y., Graham M., 2020, *MNRAS*, 495, 1958
 Wang J. et al., 2012, *MNRAS*, 423, 3486
 Weinzirl T., Jogee S., Khochfar S., Burkert A., Kormendy J., 2009, *ApJ*, 696, 411
 Westfall K. B. et al., 2019, *AJ*, 158, 231
 White S. D. M., Rees M. J., 1978, *MNRAS*, 183, 341
 Wuyts S. et al., 2011, *ApJ*, 742, 96
 Yang X., Mo H. J., van den Bosch F. C., Zhang Y., Han J., 2012, *ApJ*, 752, 41
 Zhao Y., 2012, *Ap&SS*, 337, 719
 Zolotov A. et al., 2015, *MNRAS*, 450, 2327

APPENDIX A: MASS-WEIGHTED VERSUS LUMINOSITY-WEIGHTED ROTATIONAL SUPPORTS

We show a comparison between mass-weighted λ_{R_e} and light-weighted λ_{R_e} in Fig. A1, to investigate the potential biases introduced by factors like disc fading. The mass maps are from the MaNGA FIREFLY value-added catalogue (Neumann et al. 2022). In Fig. A1, for ~ 85 per cent galaxies, the difference between these two values is

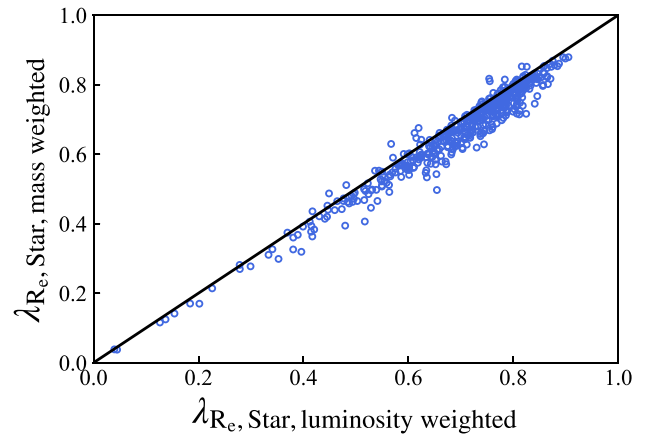


Figure A1. Mass-weighted $\lambda_{R_e, \text{Star}}$ versus light-weighted $\lambda_{R_e, \text{Star}}$. The luminosity weighted $\lambda_{R_e, \text{Star}}$ is systematically higher. A reasonable interpretation is that the outer disc component tends to have more star formation and lower mass-to-light ratio. The difference between two $\lambda_{R_e, \text{Star}}$ values generally increases as $\lambda_{R_e, \text{Star}}$ increases. The difference is up to ~ 0.1 and for ~ 85 per cent galaxies the value is up to ~ 0.06 . The difference does not affect our analysis.

less than ~ 0.06 . We also performed tests employing mass-weighted λ_{R_e} and found that our conclusions remain unaffected.

APPENDIX B: THE EFFECT OF BEAM SMEARING ON KINEMATIC MEASUREMENTS

In this section, we show that under our specific sample selection criteria (galaxies with $R_e > 5$ arcsec), the effect of beam smearing is not severe and does not bias the main conclusions. To estimate the beam smearing effect on λ_{R_e} , we adopt a simulation method which is similar to the method in Greene et al. (2018). We begin by selecting 61 galaxies with R_e larger than 10 arcsec from our primary sample. Given that the full width at half-maximum (FWHM) of the point spread function (PSF) for MaNGA is ~ 2.5 arcsec, which is half of

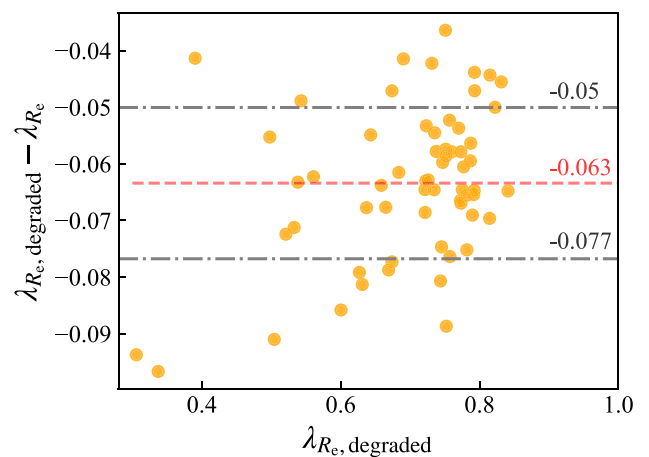


Figure B1. The difference between degraded and original $\lambda_{R_e, \text{Star}}$ versus degraded $\lambda_{R_e, \text{Star}}$ for the 61 galaxies with $R_e > 10$ arcsec in our sample. The red and grey dashed lines indicate the mean value and 1σ scatter of the y-axis. The difference between degraded and original values has a mean value of ~ -0.063 with 1σ of ~ 0.013 , and shows no dependence with the degraded values.

the lower limit of R_e in our sample, we degrade the spatial resolution of these 61 galaxies to $R_e/2$, by convolving with a Gaussian PSF with $\text{FWHM} = \sqrt{(0.5R_e)^2 - \text{FWHM}_{\text{int}}^2}$, where R_e and FWHM are both in units of arcsec. The spectrum of each pixel is simulated as a continuum plus a single Gaussian-shaped absorption line by adopting V and σ in MaNGA DAP, and the degraded V and σ maps are generated by Gaussian fitting to the new spectra.

Fig. B1 shows the difference of the degraded and the original λ_{R_e} values. Under the sample selection of $R_e > 5$ arcsec, the effect of beam smearing in underestimating $\lambda_{R_e, \text{Star}}$ is ~ 0.063 with a maximum at ~ 0.09 , and has no dependence on the degraded values. Therefore, the degradation on $\lambda_{R_e, \text{Star}}$ caused by spatial resolution is small with no bias on degraded values, and does not affect our main conclusions.

APPENDIX C: WEIGHTING OF SPECTRAL INDICES AND EMISSION-LINE EQUIVALENT WIDTHS

The spectral indices measured within apertures are luminosity-weighted mean values, where the pixel weightings are provided in MPL11 as `SPECINDEX.WGT`. To assess the validity of measuring these mean values directly from maps instead of stacking individual spectra, a comprehensive evaluation is presented in Westfall et al. (2019). In this study, we make a comparison of our D_n4000 measurements for MaNGA galaxies with those derived from integrated spectra by MPA-JHU, as illustrated in Fig. C1. An offset of ~ 0.06 is observed, which is on the order of the standard deviation (σ) in Gaussian fitting procedures. It is noteworthy that this offset is also documented in Westfall et al. (2019). We infer that it is potentially attributed to the emission line subtraction process for each pixel. The observed difference is relatively minor and does not introduce significant impact on our results.

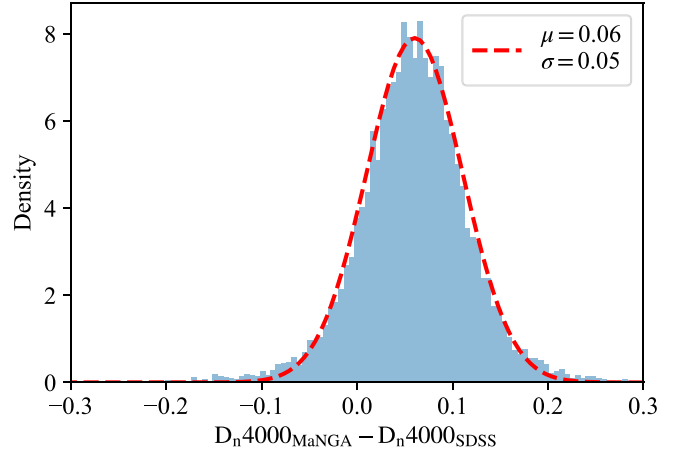


Figure C1. Histogram of the difference for D_n4000 between MaNGA central measurements within radii of 1.5 arcsec and SDSS fibre ($r = 1.5$ arcsec) measurements. The sample is the original MaNGA sample crossed matched with MPA-JHU measurements, ~ 9000 galaxies. The y-axis is density, and the labels are the mean and standard deviation of the best-fitting Gaussian. The mean value of the difference is ~ 0.06 , comparable to σ . The offset in D_n4000 is also seen in Westfall et al. (2019), and we infer that it is caused by emission-line subtraction processes for each pixel.

APPENDIX D: ROTATIONAL SUPPORT FOR H α EMISSION LINES

We test our main results with $\lambda_{R_e, \text{H}\alpha}$, which is measured for H α emission lines. Figs D1 and D2(a) and (b) are identical to Figs 4 and 6(a) and (b) with $\lambda_{R_e, \text{H}\alpha}$ measurements in substitution. $\lambda_{R_e, \text{H}\alpha}$ is systematically higher than $\lambda_{R_e, \text{Star}}$ owing to the well known trend of gas, which is dissipative, to be dynamically ‘colder’ than stars. Aside from this, the general trends consistent with stellar kinematics are reproduced.

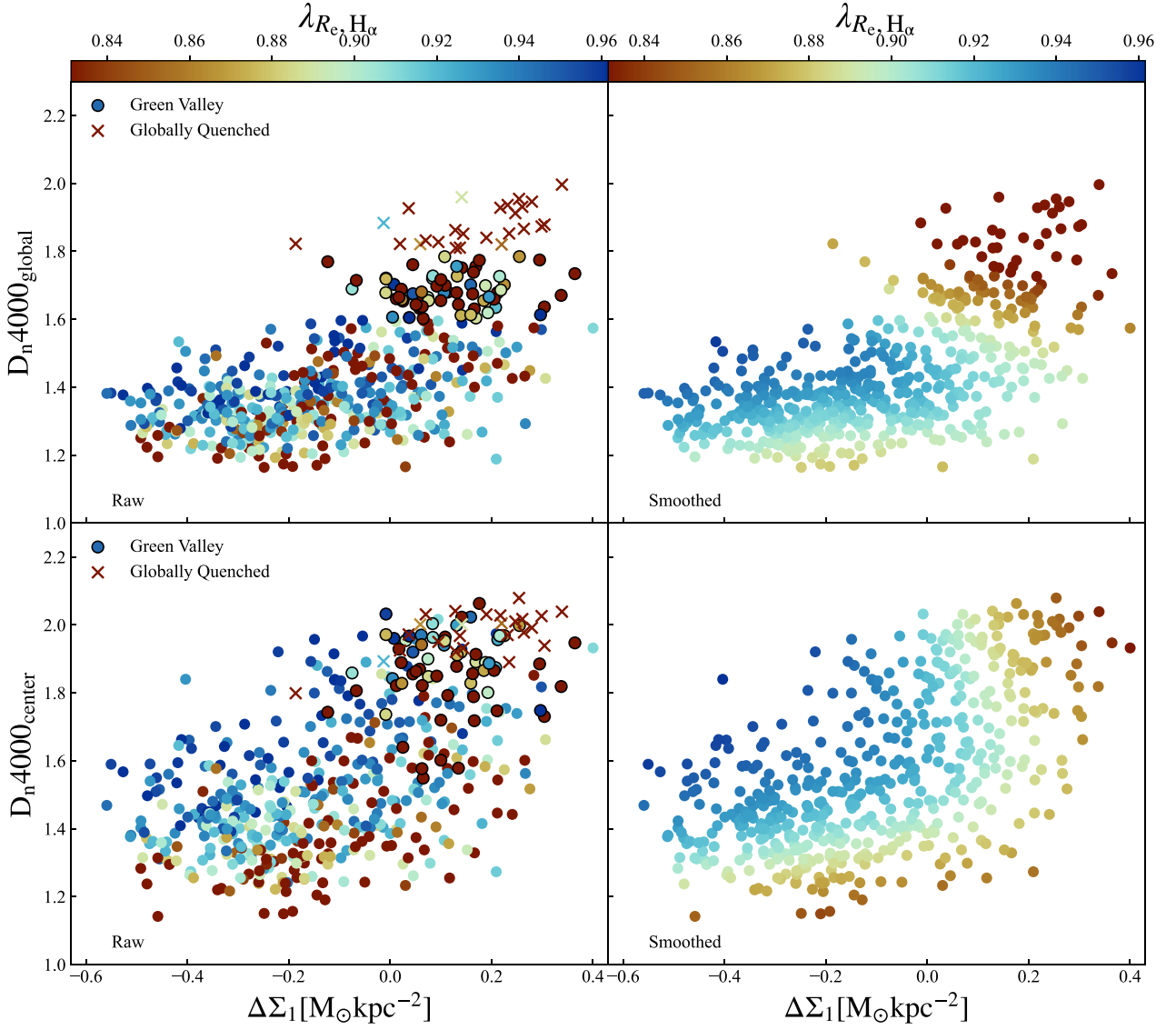


Figure D1. D_n4000_{global} and D_n4000_{centre} versus $\Delta\Sigma_1$ coloured by $\lambda_{R_{c,H\alpha}}$. The left column shows the original scatter plots and the right panels are LOESS smoothed plots. Fully quenched galaxies ($D_n4000_{\text{global}} > 1.8$) are labelled as crosses and galaxies in green valley ($1.6 < D_n4000_{\text{global}} < 1.8$) as circles with black edges. The sample is based on gas data quality (SNR of $H\alpha$ emission) and is different from Fig. 4. The distribution of $\lambda_{R_{c,H\alpha}}$ shows striped pattern in global D_n4000 versus $\Delta\Sigma_1$ and ‘J-shaped’ pattern in central D_n4000 versus $\Delta\Sigma_1$, similar to what is shown in Fig. 4.

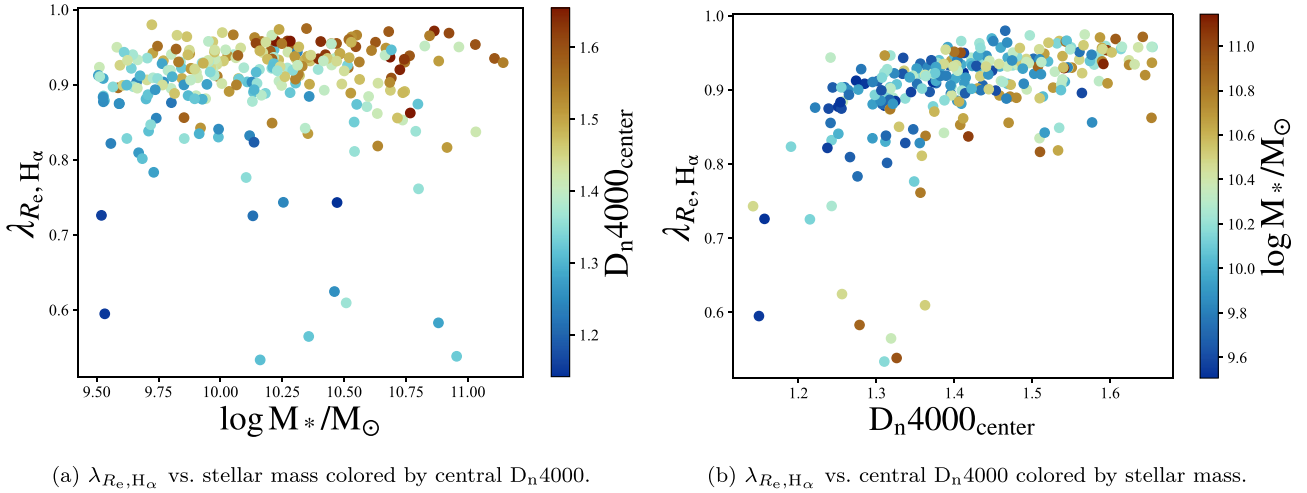


Figure D2. Replots of Fig. 6 with $\lambda_{R_e, H\alpha}$. Only galaxies with negative $\Delta\Sigma_1$ and $D_n4000_{\text{centre}} < 1.66$ are shown. The sample is based on gas data quality (SNR of $H\alpha$ emission) and is different from Fig. 6.

APPENDIX E: SAMPLE MAPS OF GALAXIES FROM DIFFERENT LOCATIONS OF STELLAR POPULATION-STRUCTURE PARAMETER SPACE

In this section, we present maps of kinematics, flux, and spectral indices for sample galaxies in Figs E1–E5. Galaxies are classified

into four types based on their locations on $D_n4000_{\text{centre}} - \Delta\Sigma_1$ plot: centrally star-forming galaxies with high $\Delta\Sigma_1$ (lower right), centrally star-forming galaxies with low $\Delta\Sigma_1$ (lower left), centrally quiescent galaxies with high $\Delta\Sigma_1$ (higher right), and centrally quiescent galaxies with low $\Delta\Sigma_1$ (higher left). We also show sample maps of low- $\Delta\Sigma_1$ galaxies with $D_n4000_{\text{centre}} < 1.3$, as they tend to have less rotational support and more disturbed morphologies.

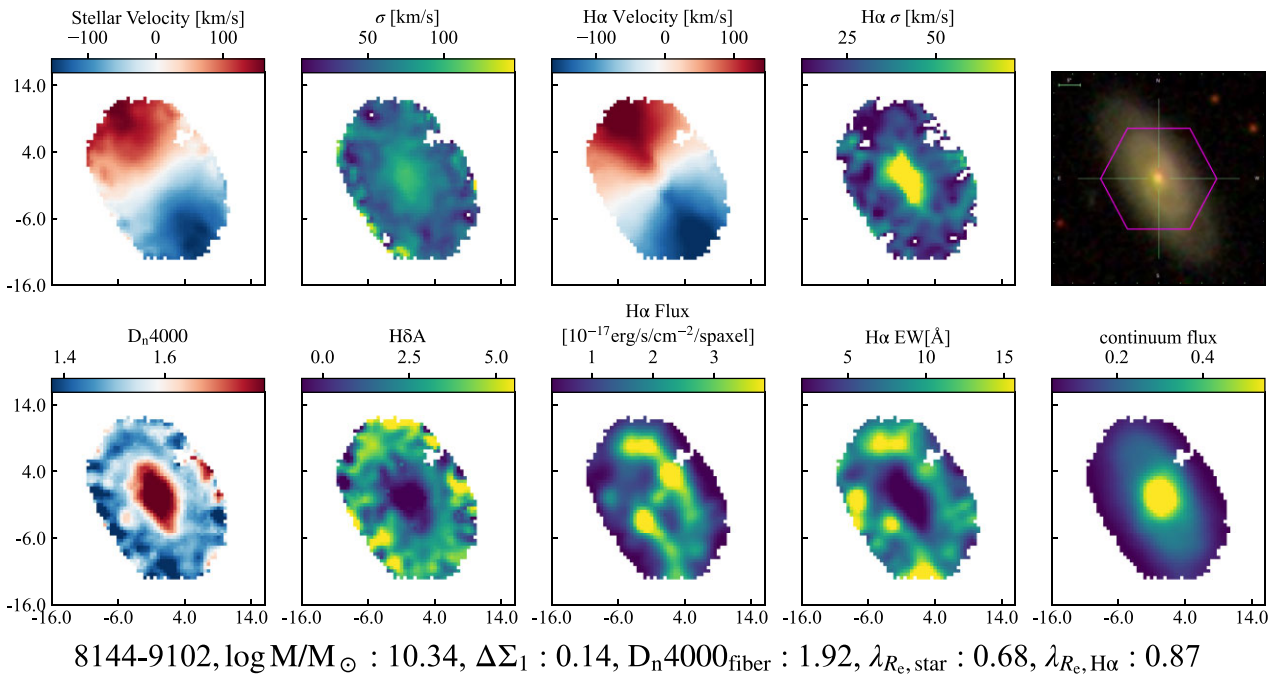


Figure E1. 8144 – 9102, an example of centrally quiescent galaxies with high $\Delta\Sigma_1$. This galaxy is also flagged as having ‘perturbed kinematics’.

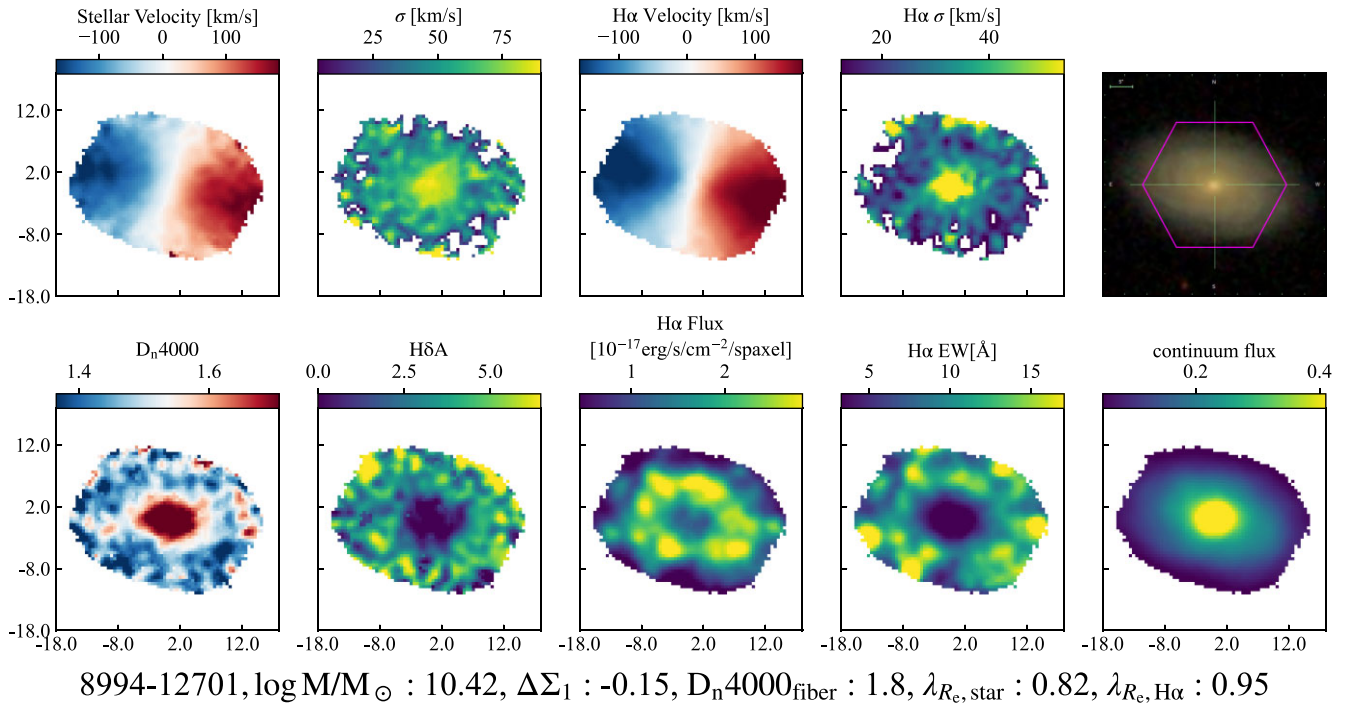


Figure E2. 8994 – 12701, an example of centrally quiescent galaxies with low $\Delta\Sigma_1$.

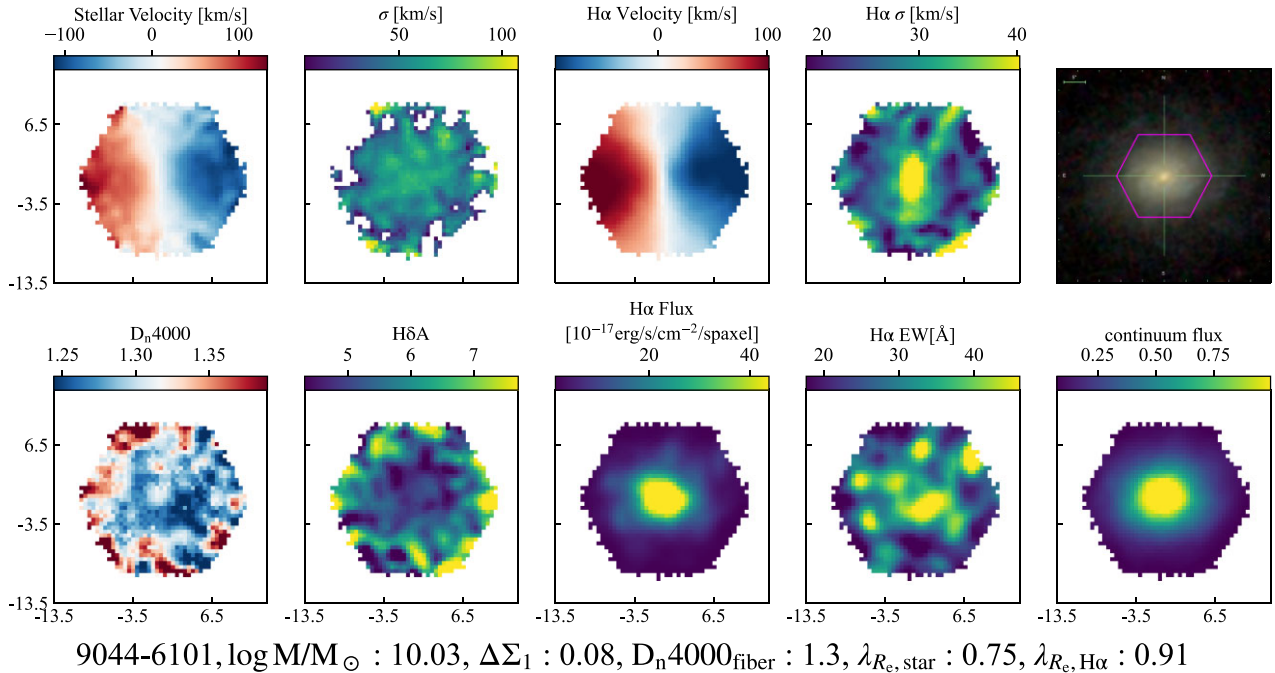


Figure E3. 9044 – 6101, an example of centrally star-forming galaxies with high $\Delta\Sigma_1$.

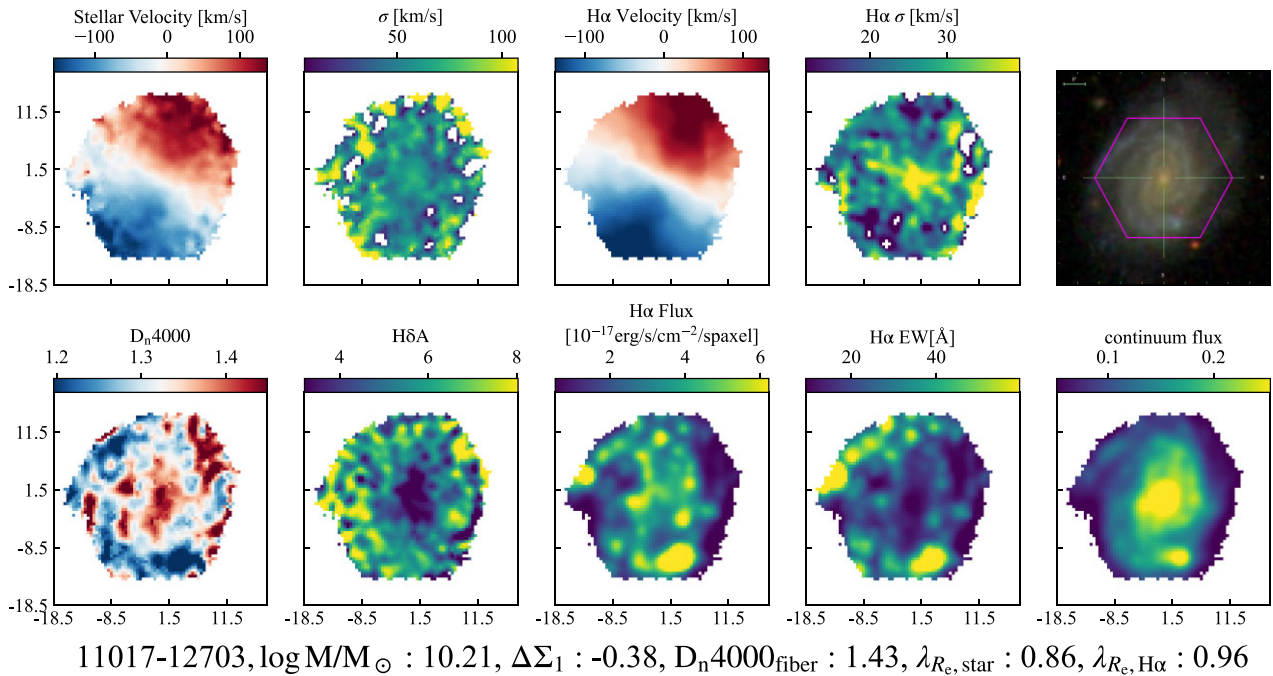


Figure E4. 11017 – 12703, an example of centrally star-forming galaxies with low $\Delta\Sigma_1$.

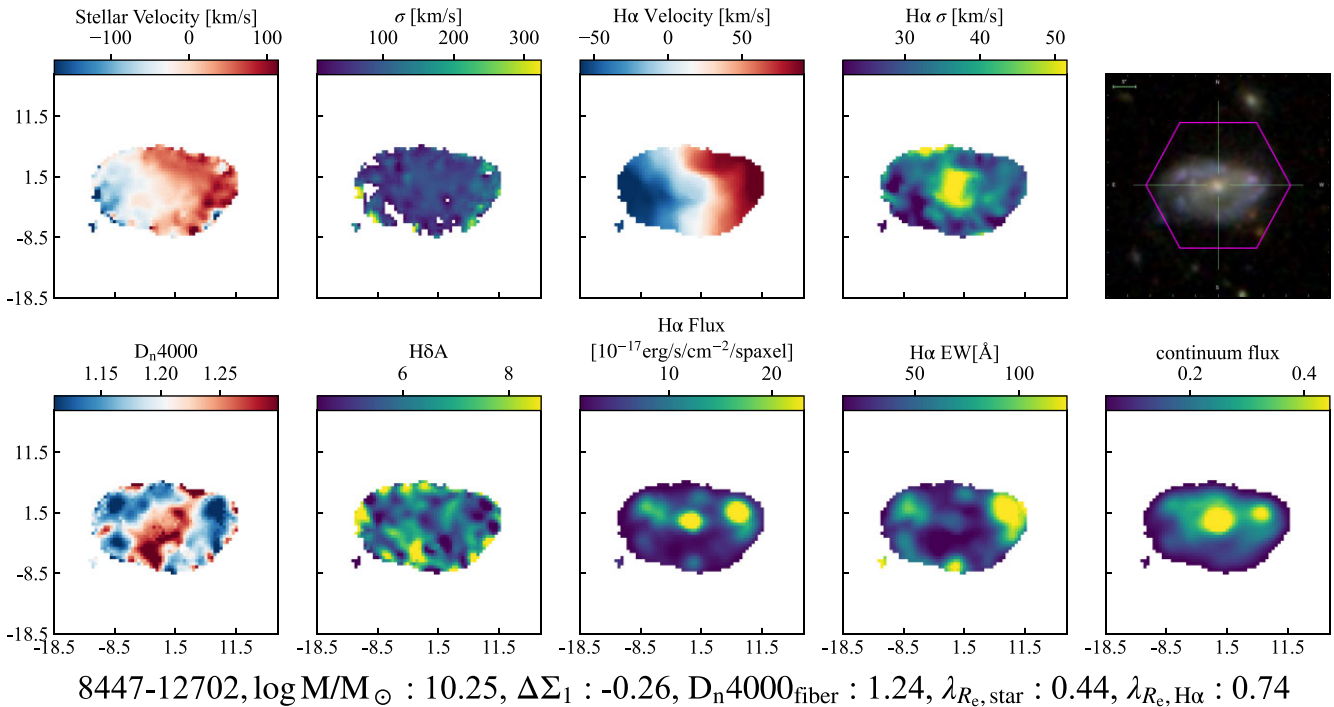


Figure E5. 8447 – 12702, an example of galaxies with low $\Delta\Sigma_1$ and very young stellar population ($D_{n4000}_{\text{centre}} < 1.3$). This galaxy is also flagged as having ‘perturbed kinematics’.

APPENDIX F: GALLERY OF LOW-CENTRAL-SURFACE-DENSITY GALAXIES WITH DIFFERENT CENTRAL STELLAR POPULATION AGES

In this section, we show an image gallery of low- $\Delta\Sigma_1$ galaxies with different central D_n4000 . Fig. F1 shows a montage of galaxies arranged by D_n4000_{centre} , with younger central stellar populations at the bottom. Galaxies on the left of the orange dividing line

are classified as having disturbed morphologies (black triangles in Fig. 7), while galaxies on the right side are from the ‘clean’ sample. The younger objects tend to show clumpier and more globally irregular, non-axisymmetric light distributions. This is consistent with the scenario we propose in Fig. 9, and also well matched by theoretical simulations of merging gas-rich galaxies, which typically show gas flows to the centre, resulting in central starbursts (Hopkins et al. 2013).

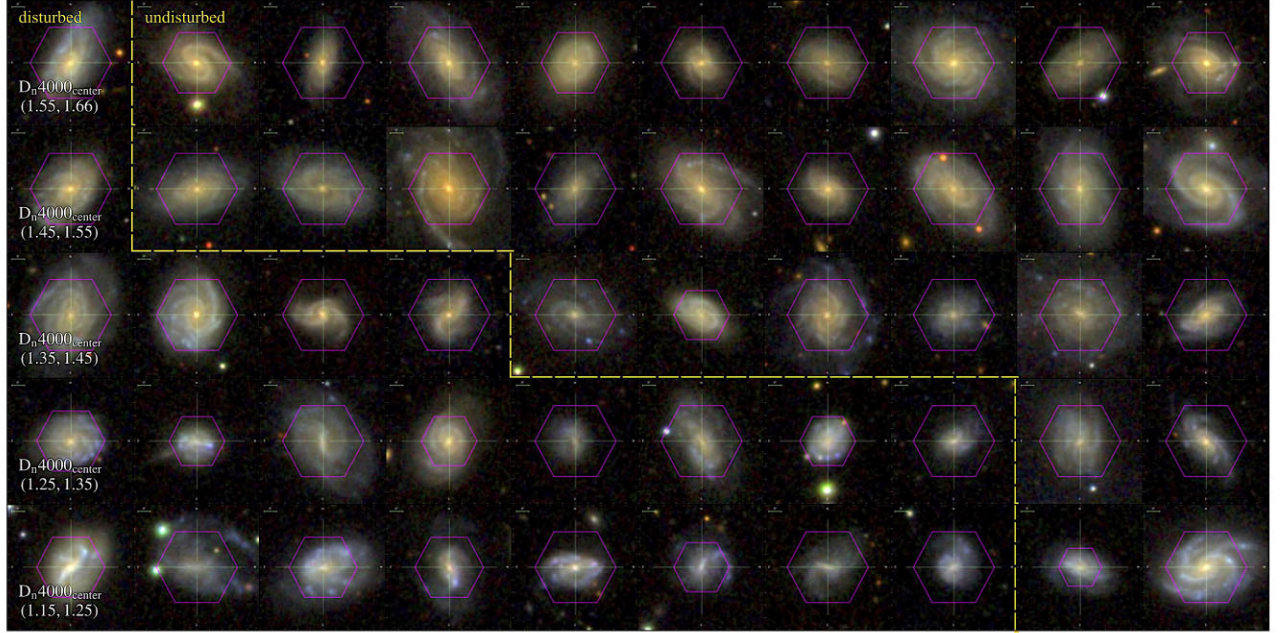


Figure F1. An image gallery of low-central-surface-density galaxies ($\Delta\Sigma_1 < 0$) with different central stellar populations and degrees of disturbance. From bottom to top are images of galaxies with D_n4000_{centre} of five bins, (1.15, 1.25), (1.25, 1.35), (1.35, 1.45), (1.45, 1.55), and (1.55, 1.66). The images left to the orange dashed line are galaxies with disturbed morphology (Section 2.3, black triangles in Fig. 7), and the images on the top right are from the clean sample (Section 2.3). From bottom to top galaxies show more and more settled and regular photometries.

This paper has been typeset from a $\text{\TeX}/\text{\LaTeX}$ file prepared by the author.